JCB Journal of Cell Biology

ARTICLE

Cellulose synthase-like D movement in the plasma membrane requires enzymatic activity

Shu-Zon Wu[1], Arielle M. Chaves[2], Rongrong Li[2], Alison W. Roberts[2], and Magdalena Bezanilla[1]

Cellulose Synthase-Like D (CSLD) proteins, important for tip growth and cell division, are known to generate β-1,4-glucan. However, whether they are propelled in the membrane as the glucan chains they produce assemble into microfibrils is unknown. To address this, we endogenously tagged all eight CSLDs in *Physcomitrium patens* and discovered that they all localize to the apex of tip-growing cells and to the cell plate during cytokinesis. Actin is required to target CSLD to cell tips concomitant with cell expansion, but not to cell plates, which depend on actin and CSLD for structural support. Like Cellulose Synthase (CESA), CSLD requires catalytic activity to move in the plasma membrane. We discovered that CSLD moves significantly faster, with shorter duration and less linear trajectories than CESA. In contrast to CESA, CSLD movement was insensitive to the cellulose synthesis inhibitor isoxaben, suggesting that CSLD and CESA function within different complexes possibly producing structurally distinct cellulose microfibrils.

Introduction

Cellulose, the major component of plant cell walls, plays essential biological roles for plants and serves important practical roles for people. In plants, cellulose is critical for morphogenesis (Bidhendi and Geitmann, 2016). For people, cellulose is a source of traditional and emerging bio-based materials (Wilson et al., 2021). Unique among land plant cell wall components, cellulose is synthesized as microfibrils, which consist of β-1,4-glucan chains joined laterally through hydrogen bonding. The mechanical properties of cellulose microfibrils depend on their cross-sectional dimensions and number of glucan chains, which in turn depend on the structure of Cellulose Synthase Complexes (CSCs) responsible for both glucan polymerization and microfibril assembly (Brown, 1996; Tsekos, 1999). The rosette-type CSCs of land plants are composed of six particles, each containing three Cellulose Synthase (CESA) catalytic subunits (Kimura et al., 1999; Mueller and Brown, 1980; Nixon et al., 2016; Pear et al., 1996; Purushotham et al., 2020; Vandavasi et al., 2016), and produce microfibrils consisting of 18 glucan chains (Jarvis, 2018; Kubicki et al., 2018; Oehme et al., 2015).

The CSC was first conceptualized in the "ordered granule hypothesis" (Preston, 1964) and posited to move in the plasma membrane (Brown et al., 1976) propelled by the force of cellulose crystallization (Diotallevi and Mulder, 2007; Herth, 1980; Roberts et al., 1982). Live-cell imaging of a YFP-CESA6 translational fusion was a critical advance that provided direct evidence of CSC movement (Paredez et al., 2006) and enabled visualization and quantification of CSC behavior (Gu and Rasmussen, 2022). While cellulose biosynthesis by CESAs has been well studied, recent evidence suggests that related Cellulose Synthase-Like D (CSLD) proteins also synthesize cellulose-like β-1,4-glucan (Hu et al., 2019; Park et al., 2011; Yang et al., 2020). Like CESAs, functional CSLDs reside in the plasma membrane (Park et al., 2011) and they synthesize β-1,4-glucan and form multimeric complexes in vitro (Yang et al., 2020). However, it is not known whether the in vivo product of CSLDs is microfibrillar.

In *Arabidopsis* and other plants, specific CSLDs are required for the development of pollen tubes (Bernal et al., 2008; Doblin et al., 2001) and root hairs (Bernal et al., 2008; Favery et al., 2001; Galway et al., 2011; Kim et al., 2007; Li et al., 2016; Park et al., 2011; Wang et al., 2001). These tubular cells direct secretion of flexible cell wall materials to their tips, allowing for a process of localized cell expansion known as polarized tip growth (Gu and Nielsen, 2013; Rounds and Bezanilla, 2013). *AtCSLD5* and its orthologs are required for normal growth of stems and leaves (Bernal et al., 2007; Hu et al., 2010; Hunter et al., 2012; Li et al., 2009; Luan et al., 2011; Wu et al., 2010; Yang et al., 2016; Yoshikawa et al., 2013). Recently, it was discovered that *atcsld5* mutants have primary defects in cytokinesis (Gu et al., 2016; Hunter et al., 2012; Yang et al., 2016) and that the gene is regulated by the cell cycle (Gu et al., 2016; Yoshikawa et al., 2013). In root hairs of *Arabidopsis*, CSLDs are tip localized,

[1]Department of Biological Sciences, Dartmouth College, Hanover, NH, USA; [2]Department of Biological Sciences, University of Rhode Island, Kingston, RI, USA.

Correspondence to Alison W. Roberts: aroberts@uri.edu; Magdalena Bezanilla: magdalena.bezanilla@dartmouth.edu.

whereas CESAs localize to subapical regions (Park et al., 2011). In cytokinesis, AtCSLD5 accumulates earlier in cell plate development than CESAs (Gu et al., 2016). These CSLD-mediated processes are also distinct in their responses to cellulose biosynthesis inhibitors (CBIs) with different modes of action (Larson and McFarlane, 2021). For example, root hair tip growth and AtCSLD3 localization are not affected by isoxaben (Park et al., 2011), which specifically targets CESA proteins (Scheible et al., 2001). In contrast, root hair tips rupture in the presence of the CBIs 2,6-dichlorobenzonitrile (DCB; Favery et al., 2001; Park et al., 2011) and CGA 325′615 (Park et al., 2011), which alter the behavior of plasma membrane localized CESAs and CSLDs (Park et al., 2011). Together these data indicate that CSLDs synthesize cellulose or a cellulose-like polymer required to maintain the integrity of growing root hairs and pollen tubes (Park et al., 2011) and contribute to the development of cell plates (Gu et al., 2016) through a process that is distinct from CESA-mediated cellulose biosynthesis.

Physcomitrium (formerly *Physcomitrella*) *patens* is typical of many mosses with a dominant haploid phase consisting of tip-growing protonemal filaments and leafy gametophores whose leaf-like structures known as phyllids are composed of cells that expand by diffuse growth (Schumaker and Dietrich, 1998). Although CESA activity is required for gametophore development (Goss et al., 2012; Scavuzzo-Duggan et al., 2015), protonemal tip growth is insensitive to the CESA-specific CBI isoxaben, but sensitive to DCB (Tran et al., 2018), which affects both CESA and CSLD proteins (Park et al., 2011). Thus, cellulose detected at the tips of growing protonemal filaments (Berry et al., 2016) may not be synthesized by CESAs. Advantages of *P. patens* as an experimental organism include CRISPR-Cas9-based methods for rapid in-locus tagging of proteins (Lopez-Obando et al., 2016; Mallett et al., 2019) and the ability to capture the continuous development of protonemata and gametophores at exquisite temporal and spatial resolution by live-cell imaging (Bascom et al., 2018; Bascom et al., 2016; Wu and Bezanilla, 2018).

It is not known whether CSLDs produce microfibrillar cellulose. However, by analogy with CESAs, this would require that CSLDs associate to form CSCs and that they move in the plasma membrane as the glucan chains produced by their enzymatic activity assemble to form microfibrils. Here, we demonstrate the roles of *P. patens CSLDs* in cytokinesis and protonemal tip growth. Using endogenous tagging, we show that the eight CSLDs localize to the apical plasma membrane in tip growing cells and to developing cell plates. We show that CSLD6 moves in linear trajectories along the plasma membrane and that this movement requires enzymatic activity, suggesting that CSLD forms complexes and synthesizes microfibrillar cellulose. Differences between CSLD6 and CESA10 in the rate, duration, and CBI sensitivity of these linear movements indicate that CSLD6 and CESA10 function within distinct structures.

Results

Moss CSLDs diversified independently from seed plants and have distinct expression patterns

A phylogenetic tree was constructed to examine the diversification of CSLDs in *P. patens* (Roberts and Bushoven, 2007); selected non-flowering plant species with sequenced genomes including the lycophyte *Selaginella moellendorffii* (Harholt et al., 2012), the liverwort *Marchantia polymorpha* (CSLD sequences identified by BLAST) and the conifer *Picea abies* (Yin et al., 2014); and angiosperms in which CSLDs have been functionally characterized including *Arabidopsis* (Richmond and Somerville, 2000), cotton (Li et al., 2017), *Populus* species, rice, and maize (Yin et al., 2014). The tree was rooted with CSLD sequences from the charophyte green alga *Coleochaete orbicularis* (Mikkelsen et al., 2014). The tree (Fig. 1) reveals that the CLSD family diversified independently in mosses, lycophytes, liverworts, and seed plants. As shown previously (Hunter et al., 2012; Pancaldi et al., 2022), seed plant CSLDs cluster in three clades that correspond to distinct mutant phenotypes related to pollen tube development (Bernal et al., 2008; Doblin et al., 2001; Moon et al., 2018; Wang et al., 2011), root hair development (Bernal et al., 2008; Favery et al., 2001; Galway et al., 2011; Hu et al., 2018; Kim et al., 2007; Li et al., 2016; Park et al., 2011; Peng et al., 2019; Penning et al., 2009; Qi et al., 2013; Wang et al., 2001; Yoo et al., 2012), and general growth effects, in some cases attributed to defects in cytokinesis (Bernal et al., 2007; Gu et al., 2016; Hu et al., 2010; Hunter et al., 2012; Luan et al., 2011; Samuga and Joshi, 2004; Wu et al., 2010; Yang et al., 2016; Yoshikawa et al., 2013; Zhu et al., 2010). The divergence of *P. patens* CSLDs into two clades, one containing CSLD2 and CSLD6 and the other containing the six remaining *P. patens* CSLDs (Fig. 1), is supported by synteny analysis (Fig. S1 A). Analysis of *P. patens* microarray data available in PEATmoss (Fernandez-Pozo et al., 2020) shows distinct expression patterns for members of these clades with *CSLD2* and *CSLD6* enriched in leafy gametophores and the others enriched in filamentous protonemata (Fig. S1 B). Overall, mRNA expression was somewhat higher for *CSLD2* than for *CSLD6*. A separate analysis of RNAseq data in PEATmoss confirmed gametophore enrichment for *CSLD2*, but *CSLD6* transcripts were not detected.

CSLD2 and CSLD6 are redundantly required for gametophore cellular patterning

To investigate functional specialization within the *P. patens* CSLD family, we used homologous recombination (Fig. S2 A) to knock out *CSLD2* (Pp3c25_12650V1.1) and *CSLD6* (Pp3c6_4060V1.1), close paralogs that are more highly expressed in gametophores. Multiple independent *csld2*KO and *csld6*KO lines (Table S1) produced protonemal colonies and gametophores with normal morphologies (Fig. 2, A–F). In contrast, the gametophores of double *csld2/6*KO lines (Table S1) had aberrant phyllids that were smaller than wild type with multiple defects related to cell expansion and cell adhesion (Fig. 2, G, and H). The mildest of these defects consists of small cell separations surrounded by cells that are elongated radially (Fig. 2, H and J), instead of parallel to the phyllid axis (Fig. 2 I). These structures were also observed occasionally in *csdl6*KO phyllids that were otherwise normal in appearance (Fig. 2 F). More severe defects observed only in *csld2/6*KOs, including bulges and tubular protrusions that appeared to form from continued expansion and division of the radially elongated cells surrounding small cell separations (Fig. 2, H and K; and Fig. S2 B), larger cell separations

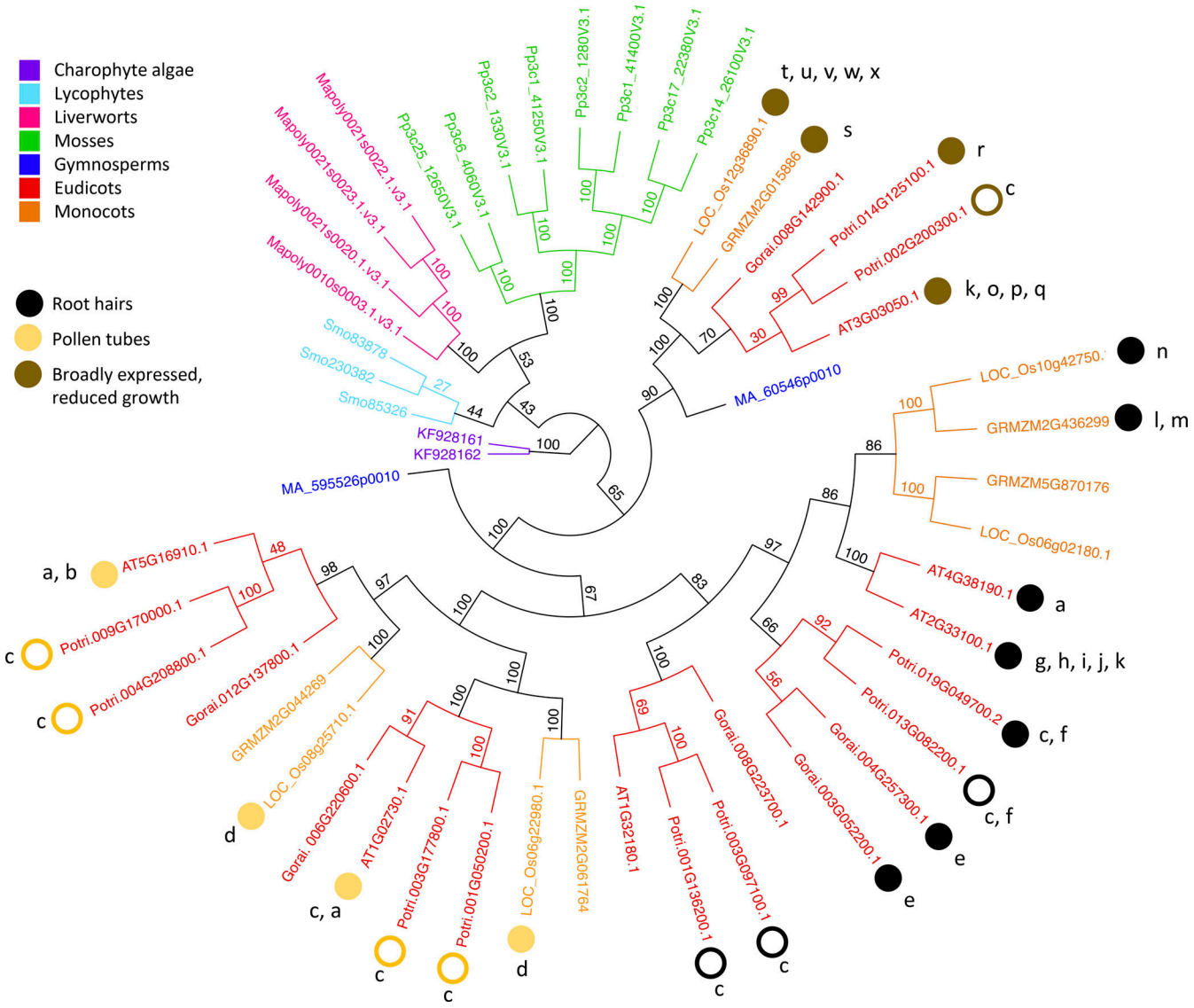

Figure 1. **Maximum likelihood cladogram of CSLD sequences from selected land plant species rooted with green algal CSLD sequences.** The CSLD families of mosses, lycophytes, liverworts, and charophyte green algae diversified independently. Angiosperm CSLDs group by demonstrated function (filled circles) and expression (open circles) with sequences from other species. Nodes are labeled with bootstrap values (1,000 replicates). Species include *Physcomitrium patens* (Pp; Phytozome locus IDs; Roberts and Bushoven, 2007), *Coleochaete orbicularis* (KF; GenBank IDs; Mikkelsen et al., 2014), *Selaginella moellendorffi* (Smo; Phytozome protein IDs; Harholt et al., 2012), *Marchantia polymorpha* (Mapoly; Phytozome; identified by BLAST), *Picea abies* (MA; Phytozome protein IDs; Yin et al., 2014), *Arabidopsis thaliana* (AT; locus IDs; Richmond and Somerville, 2000), *Populus trichocarpa* (Potri; Phytozome protein IDs; Yin et al., 2014), *Gossypium raimondii* (Gorai; Phytozome protein IDs; Li et al., 2017), *Zea mays* (GRMZM; Phytozome protein IDs; Yin et al., 2014) and *Oryza sativa* (Os; locus IDs; Yin et al., 2014). References documenting function and expression (lower case letters) are as follows: [a]Bernal et al., 2008; [b]Wang et al., 2011; [c]Peng et al., 2019; [d]Moon et al., 2018; [e]Hu et al., 2018; [f]Qi et al., 2013; [g]Favery et al., 2001; [h]Wang et al., 2001; [i]Park et al., 2011; [j]Yoo et al., 2012; [k]Yang et al., 2016; [l]Penning et al., 2009; [m]Li et al., 2009; [n]Kim et al., 2007; [o]Bernal et al., 2007; [p]Zhu et al., 2010; [q]Yin et al., 2011; [r]Samuga and Joshi, 2004; [s]Hunter et al., 2012; [t]Hu et al., 2010; [u]Wu et al., 2010; [v]Luan et al., 2011; [w]Yoshikawa et al., 2013; [x]Li et al., 2016.

(Fig. 2 L), truncated midribs (Fig. 2 M), and formation of protonema-like filaments along the phyllid margins (Fig. 2 N). Normal leaf morphology was restored when a *csld2/6*KO line was transformed with a vector driving expression of either *CSLD2* or *CSLD6* with the native promoter (Fig. S2 C).

We also examined protonemal growth in *csld2/6*KOs by morphometric analysis of colonies grown from protoplasts (Li et al., 2019; Vidali et al., 2007). In two independent experiments, we found no significant differences in plant area between wild type and any of the four *csld2/6*KO lines tested (Fig. S2 D).

CSLDs localize to cytoplasmic punctae, the apical plasma membrane of protonemal tips, and developing cell plates

To observe CSLD localization and behavior in living cells, we tagged each *CSLD* locus by inserting sequences coding for fluorescent proteins immediately upstream of the start codon (Fig. S3 A). We generated lines with the rapidly maturing form of mScarlet, mScarlet-I (Bindels et al., 2017), in a variety of strain backgrounds (Table S1). We observed fluorescent signals from all endogenously tagged CSLD lines, with all mScarlet-CSLDs localizing to cytosolic punctae. The size of the punctae

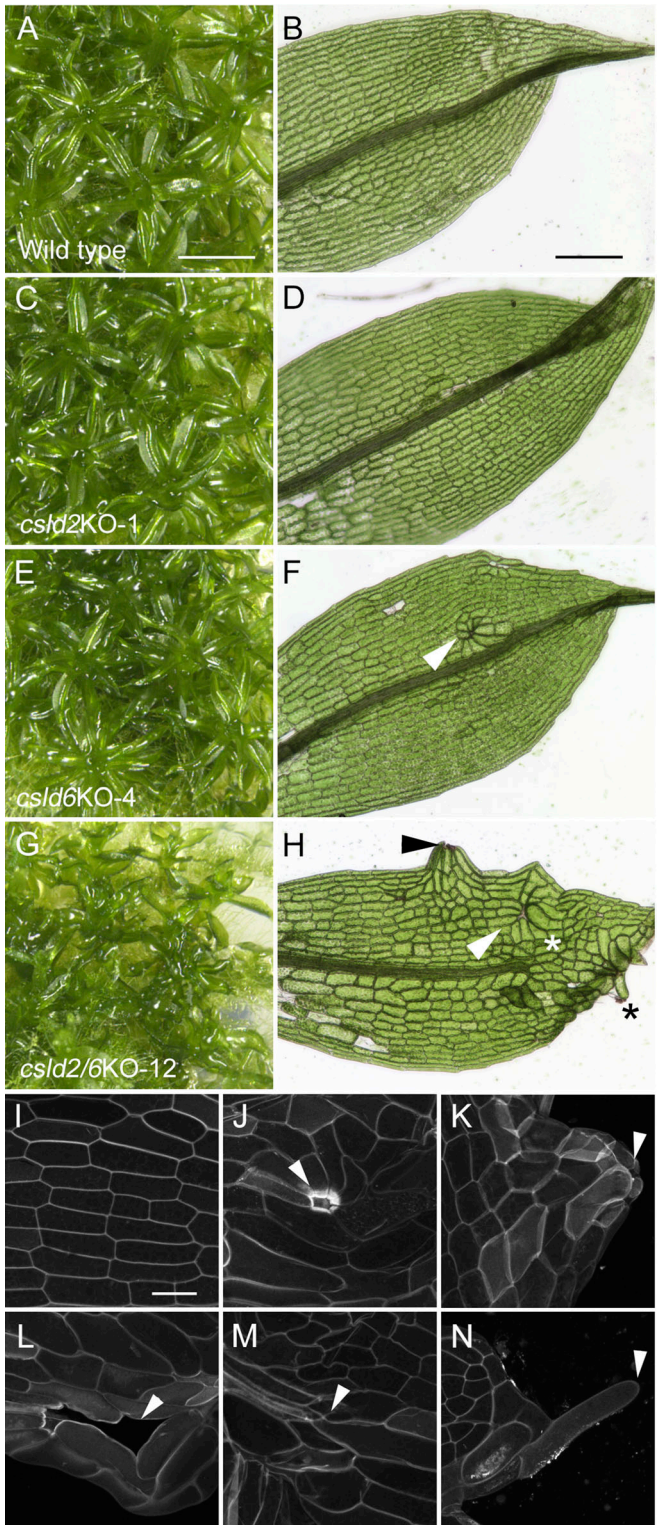

Figure 2. ***CSLD2* and *CSLD6* are redundant and required for normal phyllid development. (A and H)** Phyllid development proceeds normally in wild-type (A and B), *csld2*KO (C and D), and *csld6*KO (E and F) plants. In contrast, the phyllids of double *csld2/6*KO plants (G and H) show a variety of morphological defects including midribs that do not extend to the tips (white asterisk), formation of protonema-like filaments on the leaf margins (black asterisk) and bulges that sometimes extend to form tube-like structures (black arrowhead). Minor defects consisting of cell separations surrounded by cells with altered growth orientation (white arrowheads) are found in *csld6*KO (F) and *csld2/6*KO (H) phyllids. **(I–N)** Phyllids stained with Pontamine Fast Scarlet 4B (S4B) and imaged with confocal scanning laser microscopy. Cells elongate parallel to the phyllid axis in wild type (I). Cell adhesion and expansion defects in *csld2/6*KO plants (J–N) include structures that form where cells surrounding a small cell separation elongate in a radial pattern (J, arrowhead), bulges that form as cells surrounding a small separation elongate and divide (K, arrowhead), large cell separations (L, arrowhead), midribs that end abruptly instead of extending to the leaf tip (M, arrowhead), and marginal cells that extend as filaments that superficially resemble protonemata (N, arrowhead). Scale bars, 2 mm (A, C, E, and G), 200 µm (B, D, F, and H), and 50 µm (I and J–N).

appeared to correlate with the strength of the signal with CSLD3, 4, and 8, which had the strongest signal, containing the largest cytoplasmic punctae (Fig. 3 A). Accumulation at the apical plasma membrane was most evident in rapidly growing cells as shown for CSLD1, 3, 6, 7, and 8 (Fig. 3 A). Nevertheless, all eight CSLDs were observed on the plasma membrane in apical protonemal cells (Fig. 3 A). We also found that CSLDs accumulate on the developing cell plate (Fig. 3 B). Of the two CSLDs with predominant mRNA expression in gametophores, mScarlet-CSLD6 fluorescence was significantly stronger than mScarlet-CSLD2 (Fig. 3), suggesting that CSLD2 and CSLD6 may have differential protein stability.

To test whether N-terminal fusions impair protein function, we specifically tested mScarlet-CSLD6 functionality, because CSLD6 and CSLD2 are redundantly required for gametophore patterning and the mScarlet-CSLD6 signal was easily detectable. Since nonfunctional mScarlet-CSLD6 would disrupt gametophore patterning in the *csld2*KO background, we used CRISPR-Cas9 to disable *CSLD2* in the mScarlet-CSLD6/mEGFP-tubulin line. We found that gametophore morphology was indistinguishable from control plants for the *csld2*KO alleles we recovered in mScarlet-CSLD6 (Fig. S3 C and Table S1), demonstrating that N-terminal tagging does not disrupt CSLD6 function.

Given that all CSLDs localized similarly and that mScarlet-CSLD6 expressed robustly in both gametophores and protonemata, we studied mScarlet-CSLD6 localization and dynamics. mScarlet-CSLD6 localized to cytosolic punctae and to cell plates in gametophores (Fig. 4 A and Video 1), consistent with apparent cell division defects in *csld2/6*KO. During interphase, mScarlet-CSLD6 was relatively evenly distributed in the cytosol. However, the cytosolic punctae diminished in number and intensity as mScarlet-CSLD6 accumulated at the cell plate during cell division (Fig. 4 A, insets; Video 1). In protonemal tip cells, mScarlet-CSLD6 punctae were more concentrated toward the cell apex. However, the level of CSLD6 increased in subapical cells and it accumulated in emerging branches (Fig. 4 B and Video 2). Actin, which is essential for polarized growth, accumulates along with secretory vesicles at the apex of tip growing cells, just below the plasma membrane (Bibeau et al., 2020; Vidali et al., 2009a). Imaging of actin, labeled with lifeact-mEGFP, and mScarlet-CSLD6 revealed that CSLD6 punctae accumulate with actin at the cell tip. A sub-population of mScarlet-CSLD6 did not correlate with actin and was found to concentrate on the apical plasma membrane (Fig. 4 B, inset; Video 2). However, this membrane population disappeared when cells were treated with latrunculin B (LatB), a drug that depolymerizes the actin cytoskeleton (Fig. 4 C). These data suggest that actin is required for proper delivery of CSLD to the plasma membrane.

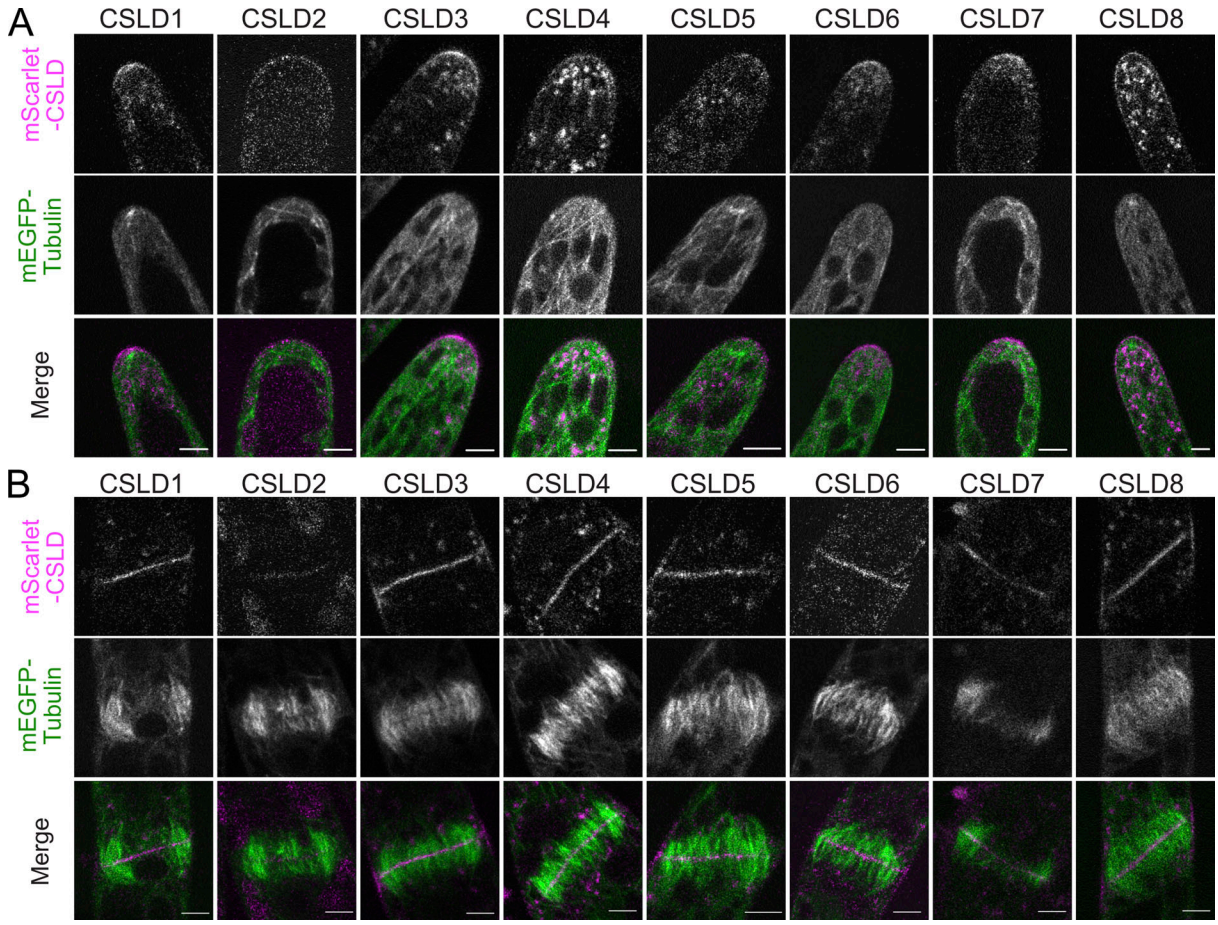

Figure 3. **Localization of endogenously tagged *CSLD1-8* with mScarlet in a moss line stably expressing mEGFP-tubulin. (A)** In protonemata, CLSDs localized to punctate structures and are enriched on the plasma membrane near the cell apex. **(B)** During cell division, CSLDs accumulate on the expanding cell plate. Scale bar, 5 µm. All images are single focal planes acquired on a laser scanning confocal microscope.

Branch initiation is an excellent model to study the molecular requirements for establishing a new site of polarized growth. Using time-lapse confocal imaging, we found that lifeact-mEGFP localizes to the presumptive branch 2 h before there is any evidence of cell expansion at that site (Fig. 4, D, and E; and Video 3), similar to previous observations that actin localizes to new polarized sites hours before expansion occurs (Wu and Bezanilla, 2018). Notably, mScarlet-CSLD6 was recruited to the same site after actin but shortly before emergence of the branch (Fig. 4, D and E; and Video 3), suggesting that CSLD activity alters cell wall properties in a way that enables expansion. In contrast to CSLD6 localization at the apical plasma membrane, we discovered that during cytokinesis mScarlet-CSLD6 accumulates in the phragmoplast midzone before actin (Fig. 4 F and Video 4), suggesting that CSLD utilizes differential delivery mechanisms during tip growth versus cytokinesis.

CSLD6 movement along linear trajectories in the plasma membrane depends on enzymatic activity and is sensitive to DCB

We used variable angle epifluorescence microscopy (VAEM) to image CSLD6 behavior at the plasma membrane. VAEM imaging uses oblique illumination to image the cell cortex below the thick cell wall, providing substantially improved signal to noise, similar to imaging animal cells with total internal reflection fluorescence microscopy. For VAEM, we tagged *CSLD6* with mEGFP (Vidali et al., 2009b; Table S1; and Fig. S3 B), which resulted in the same localization pattern as mScarlet-CSLD6 (Fig. S3 D). This allowed direct comparison to mEGFP-CESA10 (Pp3c9_2670V1.1), a CESA that is well expressed in protonemata (Tran and Roberts, 2016) and was tagged in the locus by inserting mEGFP immediately upstream of the start codon (Fig. S4, A and B). Similar to CESA5 and CESA8 (Tran et al., 2018), mEGFP-CESA10 localized to discrete dots on the plasma membrane that moved in linear trajectories (Fig. 5 A and Video 5). We found that mEGFP-CSLD6 also localized to discrete dots on the plasma membrane (Fig. 5 A and Video 5). However, in contrast to CESA10, CSLD6 had a higher density at the plasma membrane and its movements were significantly faster and shorter in duration (Fig. 5, A–C and Video 5). Quantitative analysis of CSLD6 and CESA10 particle motility by particle tracking revealed that, on average, CSLD6 particles had a wider distribution of velocities and moved significantly faster than CESA10 particles (Fig. 5 B). Notably, particle tracking speed measurements were statistically indistinguishable from kymograph measurements (Fig. 5 C). Using the particle tracking data, we

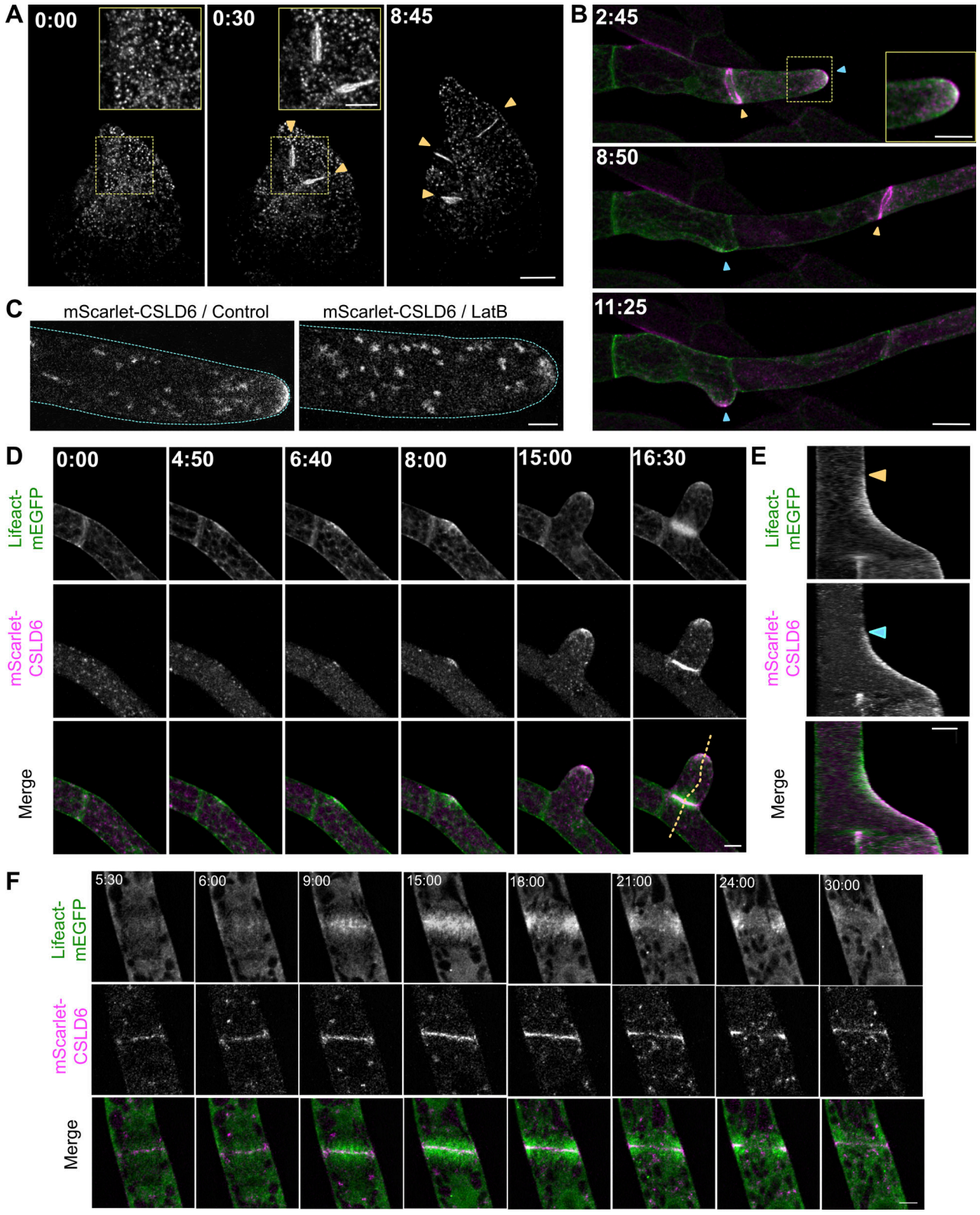

Figure 4. **Arrival of CSLD6 to the cell apex depends on and occurs after actin, but CSLD6 enrichment precedes actin at the developing cell plate.** **(A)** In moss gametophores, CLSD6 is enriched in punctate structures and in the cell plates during cell division (yellow arrowheads.) Insets from the boxed regions reveal the presence of fewer CSLD6 puncta in dividing cells. Scale bar, 20 µm. Scale bar for inset, 10 µm. Time stamps, hour:minute. Also see Video 1. **(B)** In moss protonemata, mScarlet-CSLD6 (magenta) accumulates at the cell apex (blue arrowheads) and at the site of cell division (yellow arrowheads.) Actin is labeled with lifeact-mEGFP (green), which also accumulates near the cell apex and at the site of cell division. Inset from the boxed region reveals that CSLD6 labels the plasma membrane, while actin is in the cytosol at the cell apex. Images are maximum projections of z-stacks from a time-lapse acquisition. Inset is from the medial plane. Scale bar, 20 µm. Scale bar for inset, 10 µm. Time stamps, hour:minute. Also see Video 2. **(C)** mScarlet-CSLD6 in control and LatB-

treated protonemal apical cells. Cyan dotted line outlines the cells. Scale bar, 5 µm. Images are from the medial focal plane. **(D)** During branch formation, actin appeared (4:50) before CSLD6 accumulation (6:40). Cell expansion occurs (8:00) after actin and CSLD6 accumulation. Images are maximum projections of z-stacks from a time-lapse acquisition. Scale bar, 10 µm. Time stamps, hour:minute. Also see Video 3. **(E)** Kymographs generated along the yellow dashed line in C. In the kymographs, actin appears at the cell apex (yellow arrowheads) before CLSD6 (blue arrowheads) and cell expansion. Scale bars, 10 µm (horizontal) and 2 h (vertical). **(F)** In dividing protonemal cells, CSLD6 appears in the cell plate (5:30) earlier than actin (6:00). Images are single focal plane confocal images from a time-lapse acquisition. Scale bar, 5 µm. Time stamps, min:sec. Also see Video 4.

quantified the confinement ratio, which is a ratio of the straight-line distance between the start and end point of the trajectory divided by the actual trajectory distance. The closer the ratio is to 1, the straighter the trajectory. We found that CSLD6 trajectories were significantly more circuitous than CESA10 (Fig. 5 E).

CESA trajectories at the plasma membrane result when the glucan chains generated by CESA enzymatic activity assemble to form microfibrils within the cell wall (reviewed in Pedersen et al., 2023). To test whether CSLD6 trajectories depend on enzymatic activity, we modified the mEGFP-CSLD6 locus with CRISPR and engineered a point mutation in a residue (D867N; CSLD6-TEN; Fig. S1 C and Fig. S4 C) that deprotonates the acceptor hydroxyl group and is essential for catalysis (Purushotham et al., 2016; Yang et al., 2020). VAEM imaging revealed that mEGFP-CSLD6-TEN localizes to the plasma membrane but does not move along the membrane (Fig. 5 A and Video 5), demonstrating that linear movement is dependent on enzymatic activity. Notably, the CSLD6-TEN allele exhibits gametophore patterning defects similar to the *csld2/6*KO plants (Fig. 5 D), demonstrating that CSLD6-TEN acts as a dominant negative likely resulting from lack of catalytic function.

Cellulose biosynthesis inhibitors have been used to inhibit CESAs in planta (Larson and McFarlane, 2021; Tateno et al., 2016), and in both *Arabidopsis* (DeBolt et al., 2007) and *P. patens* (Tran et al., 2018), treatment with DCB or isoxaben reduced CESA linear movements. To test whether CSLD6 movements are also sensitive to DCB and isoxaben, we used VAEM imaging and discovered that DCB treatment inhibited mEGFP-CSLD6 linear trajectories, but isoxaben treatment had no effect (Fig. 5, A, E, and F; and Video 5). In addition to not affecting the speed of CSLD6 particles, isoxaben also did not alter the confinement ratio (Fig. 5 E). This differential sensitivity to DCB and isoxaben provides a tool for distinguishing the effects of CSLD and CESA inhibition. In tip growing cells of *Arabidopsis* and *P. patens*, CSLD accumulates at the apical plasma membrane (Fig. 5 G; Park et al., 2011) and tip rupture is induced by DCB, but not by isoxaben (Fig. 5 H; Favery et al., 2001; Park et al., 2011; Tran et al., 2018). Imaging cells immediately after exposure to DCB revealed that cells accumulated CSLD6 at the apical plasma membrane before rupture (Fig. 5 H and Video 6). In contrast, isoxaben treatment did not affect CSLD6 accumulation at the tip (Fig. 5 H and Video 6) and did not affect growth or lead to cell rupture, indicating that CSLDs, but not CESAs are required for cell wall integrity at the cell apex.

To investigate whether CSLD trajectories align along cortical microtubules, we used VAEM to image mScarlet-CSLD6/mEGFP-tubulin. We found that the majority of cortical mScarlet-CSLD6 did not localize to microtubules (Fig. 6 A and Video 7). Kymograph analysis demonstrates that mScarlet-CSLD6 linear trajectories occur in the absence of microtubules (Fig. 6, B and C), suggesting CSLD trajectories are independent of microtubules.

Taken together, these data indicate important facets of CSLD6 activity. First, the dependence of CSLD6 movement on enzymatic activity suggests that CSLD synthesizes a fibrillar polymer at the plasma membrane. Second, the differences in speed, duration, pathway, CBI sensitivity, and microtubule dependence of CESA10 and CSLD6 trajectories suggest that these proteins do not co-assemble, and that CSLDs synthesize fibrils at a faster rate and in a less constrained pattern compared to CESAs. Thus, CSLDs and CESAs function in distinct complexes, or CSCs, with different developmental functions.

CSLDs strengthen the developing cell plate

To probe CSLD function during cytokinesis, we used cells that express mScarlet-CSLD6 along with a microtubule marker (mEGFP-tubulin), and we stained for callose (using aniline blue) as a cell plate marker. We imaged cytokinesis in protonemata to take advantage of superior temporal and spatial resolution that can be achieved in these cells and used DCB treatment to examine the effects of acute inhibition of CSLD activity during cell division. Given that all CSLDs localize to the developing cell plate in protonemata, DCB was used to effectively inhibit cytokinesis by reducing all CSLD activity. During cell division, CSLD6 began accumulating in the midzone of early phragmoplasts. Fully expanded phragmoplasts exhibited maximal CSLD6 signal (Fig. 7 A, 20:00). As the aniline blue signal increased, we observed a concomitant decrease in CSLD6 (Fig. 7 A, 30:00), showing that it functions in early stages of cytokinesis before callose accumulates (Fig. 7 A and Video 8). Although DCB had no effect on the timing of mScarlet-CSLD6 accumulation during phragmoplast expansion, we observed that fully expanded phragmoplasts were deformed, often bending in the middle (Fig. 7 B, 18:00 to 25:00), but subsequently flattening out as callose accumulated (Fig. 7 B, 35:00 and Video 8). Like inhibition of CSLD movement (Fig. 5 A) and tip rupture (Fig. 5 H; Tran et al., 2018), phragmoplast bending was observed only with DCB treatment and not with isoxaben treatment (Fig. S5 A), which inhibits CESAs, and not CSLD. Together, these results suggest that CSLD activity contributes to the structural integrity of the nascent cell plate during phragmoplast expansion. Eventually, the DCB-treated cell plates straighten (Fig. 7 B and Video 8) indicating stabilization by other cell wall components.

Both microtubules and actin filaments have been hypothesized to direct vesicle trafficking as well as influencing cell plate positioning and structural stabilization (Smertenko et al., 2017). This proposed role in reinforcing the nascent cell plate prompted us to test whether actin contributed to straightening the bent

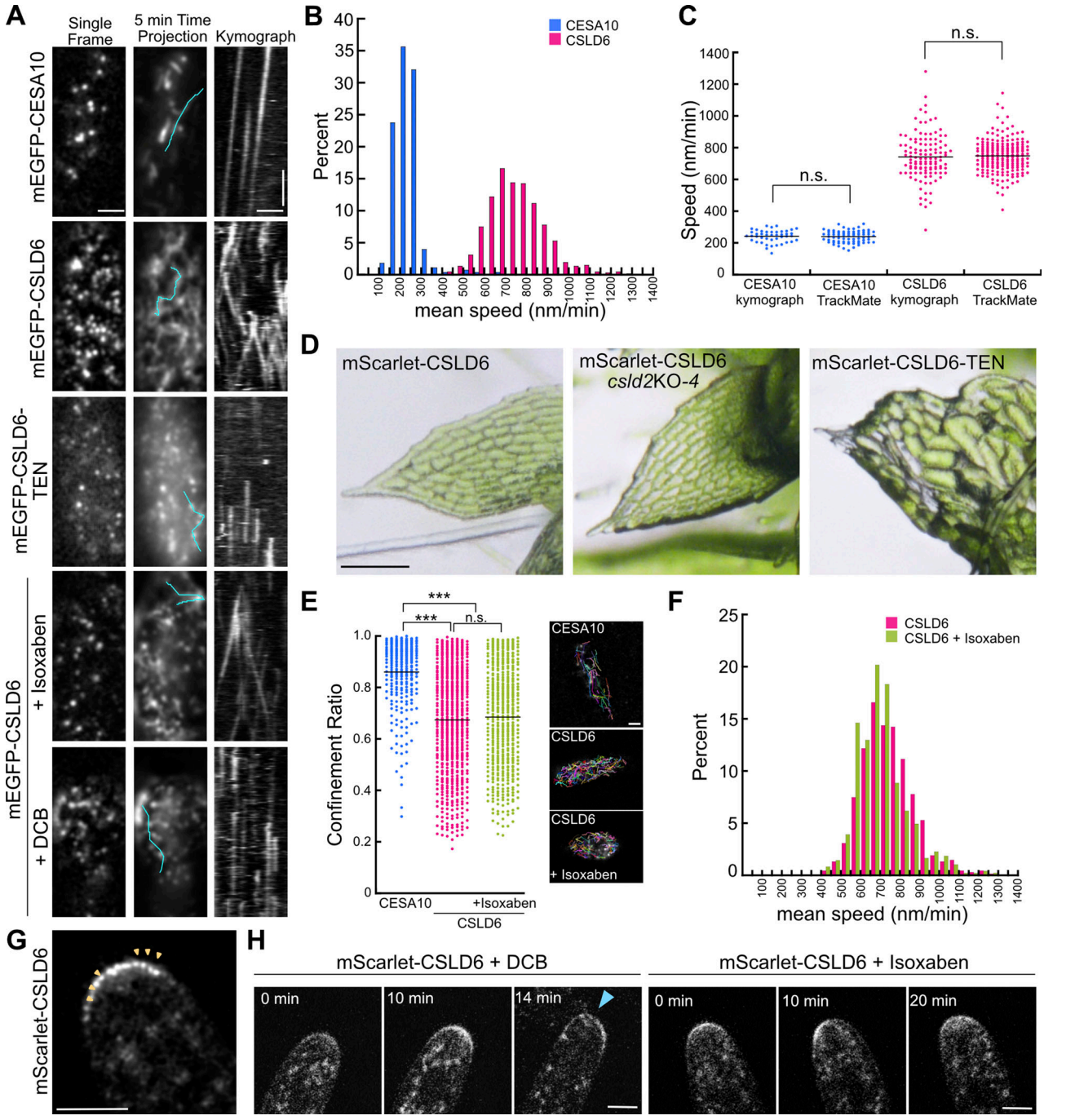

Figure 5. **CSLD6 moves in linear trajectories on the plasma membrane, which are specifically inhibited by DCB. (A)** Moss protonemata expressing mEGFP-CESA10, mEGFP-CSLD6, or mEGFP-CSLD6-TEN imaged with VAEM. mEGFP-CSLD6-TEN did not move in the membrane. 20 µM isoxaben did not affect CSLD6 particle movement, but treatment with 10 µM DCB treatment inhibited CSLD6 particle motility. Scale bar for all images in A, 2 µm (horizontal) and 1 min (vertical). Kymographs were generated along a trajectory in the time projection. Also see Video 5. **(B)** Histogram of particle speed as determined by particle tracking with the Fiji plugin TrackMate. On average CSLD6 particles moved faster than CESA10. **(C)** Speed measurements from kymographs (CESA10, *n* = 44 trajectories from two cells; CSLD6, *n* = 119 trajectories from two cells) or from particle tracking (CESA10, *n* = 72 trajectories from two cells; CSLD6, *n* = 198 trajectories from two cells) were the same. n.s. denotes no significant difference as determined by a Kruskal–Wallis statistical test. **(D)** Images of phyllids from gametophores of the indicated genotype show that the CSLD6-TEN allele (containing the D867N mutation) exhibits abnormally shaped cells similar to phyllids from *csld2/6*KO plants (see Fig. 2). Scale bar for all images in D, 100 µm. **(E)** Confinement ratio shows that CESA10 trajectories from ten cells were straighter than CSLD6 trajectories (CESA10, *n* = 271 from ten cells; CSLD6, *n* = 682 trajectories from five cells, CSLD6+isoxaben, *n* = 486 trajectories from six cells). Asterisks denote P < 0.001 and n.s. denotes no significant difference as determined by a Kruskal–Wallis statistical test. Scale bar for all images in E, 2 µm. **(F)** Histogram of CSLD6 particle speed with or without isoxaben treatment as determined by particle tracking with the Fiji plugin TrackMate. **(G and H)** Single focal plane confocal time-lapse image of protonemata expressing mScarlet-CSLD6 with no drug (G), 20 µM DCB, or 20 µM isoxaben (H). Scale bar for all images in G and H, 5 µm. Also see Video 6. **(G)** CSLD6 accumulated at the cell apex and appeared as punctae (yellow arrowheads). **(H)** With DCB treatment, CSLD6 still accumulated at the cell apex but the tip cell ruptures (blue arrowhead). Isoxaben treatment did not cause cell rupture and did not affect CSLD6 localization to the cell tip.

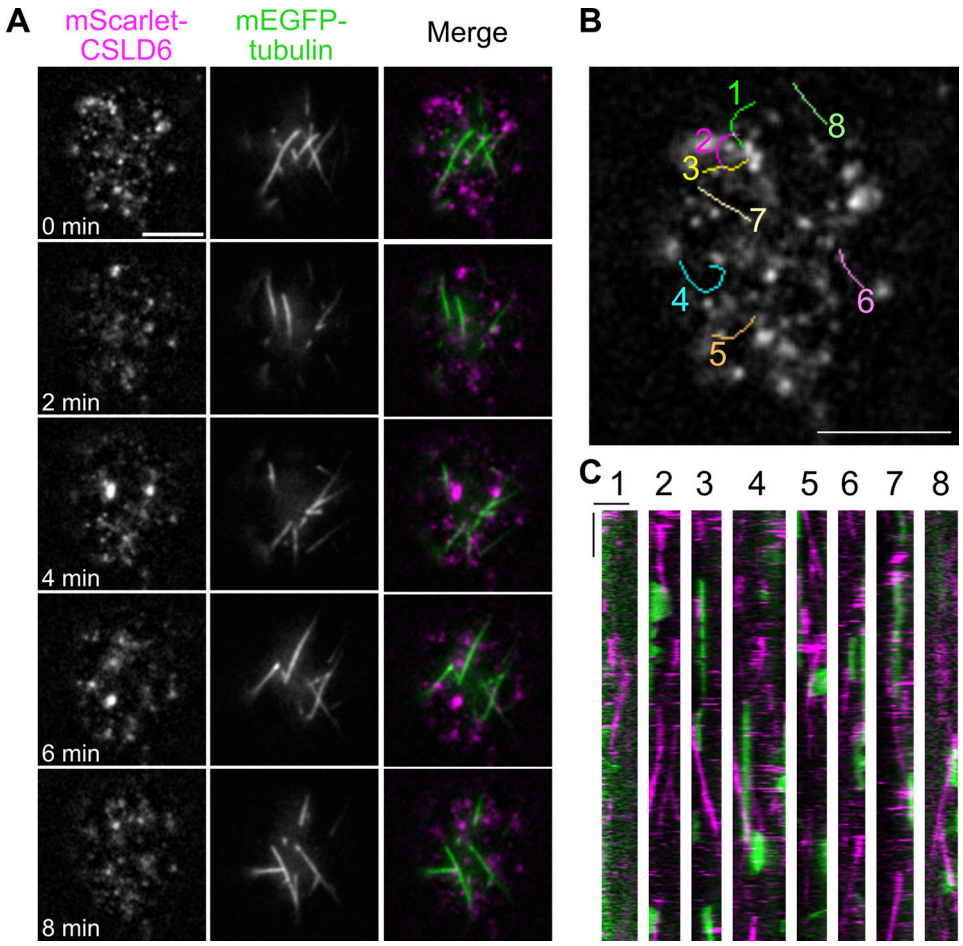

Figure 6. **CSLD trajectories do not align with cortical microtubules. (A)** Time-lapse VAEM imaging of protonemata expressing mScarlet-CSLD6 (magenta in the merged image) and mEGFP-tubulin (green in the merged image) demonstrate that the majority of CSLD6 particles do not associate with cortical microtubules. Scale bar for all images in A, 5 µm. Also see Video 7. **(B and C)** Lines on the image were used to produce the kymographs shown in C. Scale bar in B, 5 µm. **(C)** Kymographs demonstrate that mScarlet CSLD6 (magenta) moves in linear trajectories that are not associated with microtubules (green). Horizontal scale bar in C, 2 µm. Vertical scale bar in C, 1 min.

cell plates in DCB-treated cells. Depolymerizing actin with LatB had no effect on the timing of CSLD6 accumulation at the cell plate (Fig. 7 C and Video 9). These data are consistent with the dynamics of CSLD6 and actin accumulation at the phragmoplast (Fig. 4 F), and demonstrate that CSLD6 recruitment to the nascent cell plate does not depend on actin. Division proceeded relatively normally in LatB-treated apical cells (Fig. 7 C and Video 9). While difficult to represent in still images, we did notice that the CSLD6 signal appeared wavier during cell plate maturation in LatB-treated cells (Video 9), suggesting that the nascent cell plate might be slightly less able to maintain structural integrity without actin.

Notably, treatment with both LatB and DCB caused more substantial cell plate destabilization than either LatB or DCB treatment alone (Fig. 7, B–D; and Videos 8, 9, and Video 10). LatB did not affect the timing of DCB-induced deformation of cell plates labeled with mScarlet-CSLD6, which still began when the phragmoplast microtubules reached the cell cortex (Fig. 7 D, 5:00). However, without actin, the cell plates did not flatten out and continued to buckle and twist, ultimately appearing to partially fragment (Fig. 7 D 10:00–25:00, Video 10). Depolymerization of phragmoplast microtubules was delayed (Fig. 7 D 35:00–45:00, Video 10). Callose staining occurred later than in controls and was uneven (Fig. 7 D, 80:00, Video 10). In contrast to DCB, isoxaben did not enhance LatB destabilization of cell plates (Fig. S5 B), further supporting that CESA activity does not contribute to strengthening the nascent cell plate. Dramatic defects in cell plate formation induced by acutely inhibiting CSLD and actin suggest that CSLD and actin redundantly function to stabilize the nascent cell plate during cell plate expansion.

Discussion

CSLD movement in the plasma membrane is consistent with complex formation and microfibril synthesis

Earlier suggestions that CSLDs form complexes and synthesize microfibrillar cellulose were based on several types of indirect evidence and in vitro studies. Cellulose is required to maintain tip integrity in root hairs, and growing evidence indicates that this cellulose is synthesized by CSLDs (Galway et al., 2011; Gu and Nielsen, 2013; Park et al., 2011; Yang et al., 2020). Cellulose deposited at the tips of root hairs is fibrillar (Mulder et al., 2004)

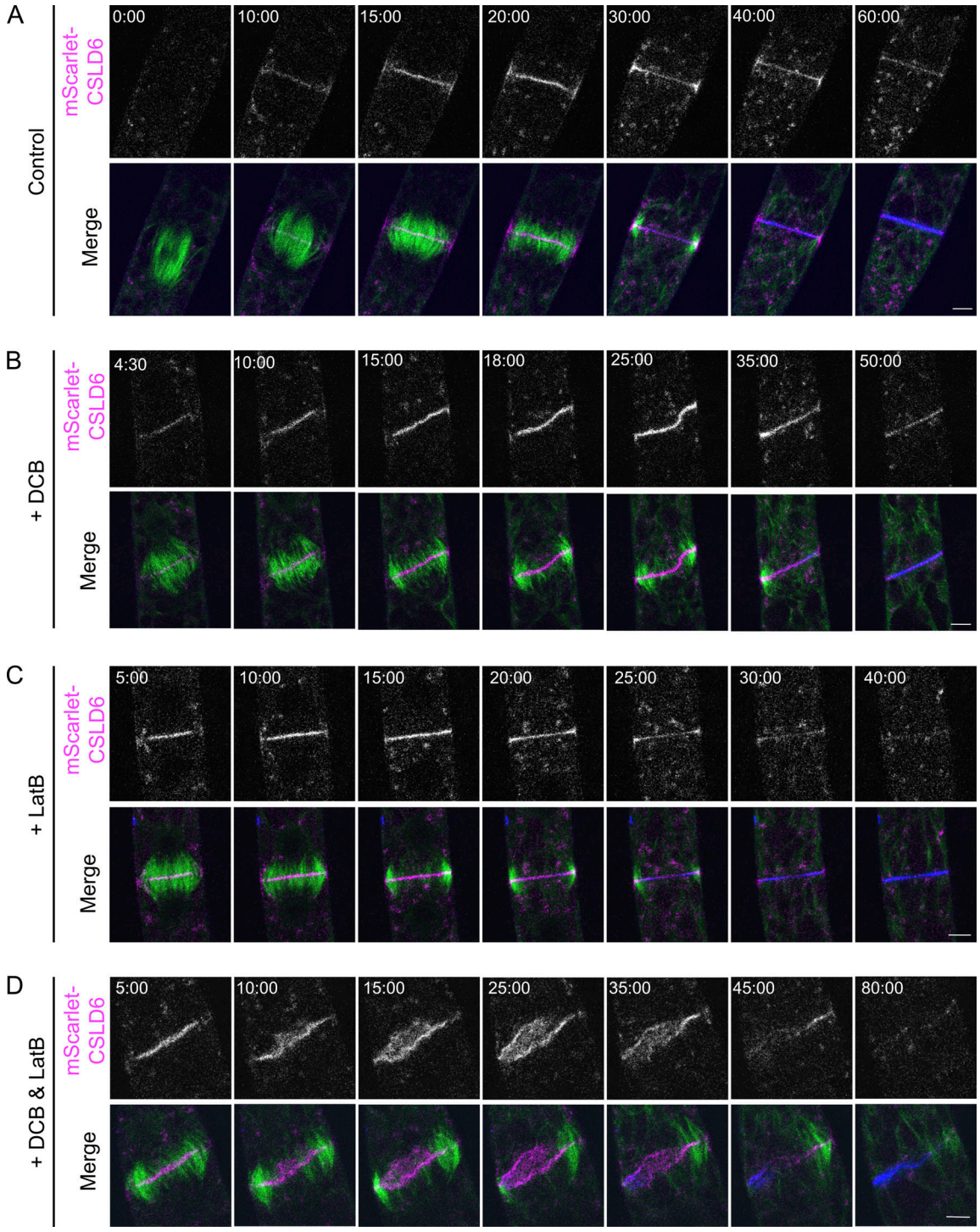

Figure 7. **CSLD activity and actin stabilize the nascent cell plate.** Cell divisions in moss protonemata expressing mScarlet-CSLD6 (magenta in merge) and mEGFP-tubulin (green in merge) and stained for callose with aniline blue (blue in merge). **(A)** Cell without drug treatment. Also see Video 8. **(B)** Cell treated with 10 µM DCB. The cell plate buckles (18:00 and 25:00) but straightens again afterward (35:00 and 50:00). Also see Video 8. **(C)** Cell treated with 25 µM LatB. Also see Video 9. **(D)** Cell treated with 25 µM LatB and 10 µM DCB. Also see Video 10. Scale bars, 5 µm. Time stamps, min:sec.

and root hair tip growth was disrupted when assembly of these microfibrils was inhibited by recombinant cellulose binding domains (Shpigel et al., 1998). Mutating one of the two CSLDs required for root hair tip integrity resulted in a patchy distribution of cellulose suggestive of disruption of microfibril assembly (Galway et al., 2011), possibly because CSLD complex formation was blocked. More recently, particles resembling the lobes of rosette CSCs were detected in CSLD reaction mixtures demonstrating that CSLDs form complexes in vitro, although fibrils were not detected (Yang et al., 2020). CSLD complex

formation is also suggested by intragenic complementation of the *csld1* mutant phenotype in *Lotus japonicus* (Karas et al., 2021). The possibility that CSLDs move in the plasma membrane was suggested based on the premise that DCB-induced expansion of the tip-localized AtCSLD3 zone in root hairs is attributable to inhibition of tip-directed CSLD movement (Park et al., 2011). VAEM imaging of GFP-CSLD6 in *P. patens* protonemata (Fig. 5; Videos 4 and 5) provides direct evidence that CSLDs move in linear trajectories along the plasma membrane. Further, mutation of a conserved residue required for catalysis (Purushotham et al., 2016; Yang et al., 2020) inhibits CSLD movement, demonstrating its dependence on enzymatic activity. By analogy with CESAs (Diotallevi and Mulder, 2007), we postulate that this movement results from the production of microfibrils that upon incorporation into the cell wall, propel the CSLD6 in the plane of the membrane. A structurally distinct CSC formed by CSLDs instead of CESAs could synthesize microfibrillar cellulose with distinct properties that facilitate tip growth and cytokinesis.

CESA and CSLD function independently

Chimeric proteins consisting of AtCSLD3 with its catalytic domain replaced by the AtCESA6 catalytic domain can rescue the *atcsld3* root hair growth phenotype (Park et al., 2011). Conversely, a chimera of AtCESA6 with the catalytic domain of AtCSLD3 can rescue the *atcesa6* null phenotype and moved in the plasma membrane as part of a complex that also contained AtCESA3. These data indicate that regions outside the catalytic domain of these proteins are responsible for their distinct functions, including complex formation, fibrillar structure of the product, and subcellular targeting (Yang et al., 2020), but they do not rule out the possibility that CESAs and CSLDs associate with one another to form mixed CSCs. We show that CSLD6 movements are faster and shorter in duration as compared to CESA10 and are not inhibited by isoxaben (Fig. 5; and Videos 4 and 5). These distinct patterns of movement are consistent with the hypothesis that CSLD6 and CESA10 function within distinct CSCs and produce microfibrillar cellulose at different rates. This is consistent with previous observations that CESA and CSLD function is separated in time and space. In root hairs, eGFP-AtCESA6 localization is subapical (Park et al., 2011) and CESAs have been assigned a role in deposition of the helicoidal cell wall that is deposited in the non-growing shank (Emons, 1994; Lindeboom et al., 2008). In contrast, CSLDs are localized to the tips of both *P. patens* protonemata (Figs. 3, 4, and 5) and *Arabidopsis* root hairs (Park et al., 2011). GFP-AtCESAs are more abundant in the late stages of cell plate maturation (Fujita and Wasteneys, 2014; Gu et al., 2016; Miart et al., 2014), whereas CSLDs are present in the early cell plates in *P. patens* (Figs. 3, 4, and 7) and *Arabidopsis* (Gu et al., 2016).

CESA/CSLD diversification

Phylogenetic analysis confirms that the *CSLD* families of mosses and seed plants diversified independently from a single ancestral gene (Fig. 1; Pancaldi et al., 2022). CSLD families from both lineages include members that function in tip growth and cytokinesis, suggesting that both functions are ancestral. In the seed plant lineage, CSLD orthologs from *Arabidopsis* and rice have similar expression patterns in pollen (Bernal et al., 2008; Moon et al., 2018; Wang et al., 2011), root hairs (Bernal et al., 2008; Kim et al., 2007), or in dividing cells (Gu et al., 2016; Yang et al., 2016; Yoshikawa et al., 2013) indicating that subfunctionalization (i.e., evolution of differential expression patterns resulting from promoter modification) preceded the divergence of monocots and eudicots. In *P. patens*, the two CSLD clades are distinguished by preferential expression in gametophores or protonemata (Figs. S2 and S3) indicating that subfunctionalization preceded the first whole-genome duplication. In *Arabidopsis*, single *csld* mutations have distinctive phenotypes, consistent with limited redundancy (Hunter et al., 2012), although analysis of double and triple mutants showed some overlapping function (Yang et al., 2016; Yin et al., 2011).

Role of CSLD in tip growth, cell division, and cell expansion

Here, we show that *P. patens* CSLDs are associated with both tip growth and cytokinesis. First, all CSLDs localize to protonemal cell tips and to cell plates (Fig. 3). Second, inhibiting CSLD function with DCB-induced tip rupture (Fig. 5; and Videos 4, 5 and 6), and destabilized developing cell plates (Fig. 7; and Videos 7, 8, 9 and 10). Similar to catalytic inactivation of CSLD6, DCB inhibited mEGFP-CLSD6 movement in the plasma membrane, demonstrating that DCB inhibits CSLD function. Notably, CSLD stabilization of the nascent cell plate is synergistic with actin. Acute inhibition of either CSLD or actin did not dramatically alter cytokinesis (Fig. 7). However, acute inhibition of both CSLD and actin resulted in cytokinesis failure (Fig. 7), suggesting that CSLD helps maintain the structural integrity of the cell plate, while actin helps to anchor the membranous network containing the developing cell plate to the plasma membrane. Although catalytic inactivation of CSLD6 did not result in loss of protonemal tip integrity, we did observe a dominant negative phenotype in mEGFP-CSLD6-TEN gametophores that resembles the *csld2/6*KO phenotype. This confirms that mEGFP-CSLD6-TEN is inactive and is also consistent with low expression of CSLD6 in protonemata relative to other CSLDs. Isoxaben, which specifically targets CESAs (Scheible et al., 2001), had no effect on any of these processes, suggesting that the effects of DCB are attributable to CLSD inhibition. Collectively, these data support the hypothesis that the product of CSLD activity stabilizes nascent cell walls formed during tip growth and cytokinesis in *P. patens*.

Mutation analysis revealed that the gametophore-enriched CSLDs, CSLD2, and CSLD6, function redundantly to maintain normal phyllid development. Although *csld2*KOs and *csld6*KOs have little or no obvious phenotype, double *csld2/6*KOs produce aberrant phyllids with defects in cell adhesion and patterning. Many of the cell patterning defects appear to result from changes in the direction of expansion of cells directly adjacent to cell separations (Fig. 2). The separations almost certainly alter the stress-strain relationships between adjacent cells, and it is known that plant cells alter their direction of cell expansion in response to mechanical signals (Hamant and Haswell, 2017). Thus, the patterning defects observed in phyllids may be an indirect consequence of cell separation, resulting from altered tissue mechanical forces and consequent changes in the polarity of cell expansion.

Mutations that affect *AtCSLD5* or its orthologs in other seed plants also alter cell patterning (Gu et al., 2016; Hunter et al., 2012; Yang et al., 2016; Yoshikawa et al., 2013). Effects include epidermal bulges on maize leaves that superficially resemble the bulges we observed on moss phyllids (Hunter et al., 2012) and enlarged and misshapen bulliform, bundle sheath, and stomatal lineage cells in rice (Yoshikawa et al., 2013). These data suggest that CSLD impairment may impact cell expansion. Interestingly, Yang et al. (2016) reported linkage composition changes for all polysaccharide classes in the meristems of *Arabidopsis csld* mutants. Compensatory alteration of cell wall composition is a common response to chemical or genetic inhibition of cellulose synthesis that is thought to be mediated by a cell wall integrity sensing system (Anderson and Kieber, 2020). This response may underly the varied developmental defects that result from *csld* mutations in *P. patens* and other plant species.

Localization of all CSLDs to protonemal cell tips and cell plates suggests that *CSLDs* function redundantly in protonemata. Live-cell imaging experiments employing lines expressing lifeact-mEGFP along with mScarlet-CSLD6, as a representative CSLD, showed that actin accumulates 1–2 h before CSLD at new tip growth sites. Notably, cell expansion was not detected until CSLD6 was recruited to the growth site, suggesting that CSLD6 activity is in part required to produce extensible cell walls. Furthermore, actin depolymerization with LatB demonstrated that actin maintains CSLD6 accumulation at cell tips during growth, similar to previous observations in *Arabidopsis* root hairs (Park et al., 2011). In contrast during cell division, CSLD6 accumulates in the phragmoplast before actin and in the presence of LatB, suggesting that actin-independent trafficking recruits CSLD6 to the developing cell plate. During cell division, actin instead helps to strengthen the cell plate during expansion. Our data demonstrate that the same protein is trafficked via actin-dependent and -independent pathways to distinct subcellular sites, the cell tip, and the phragmoplast. Ultimately, CSLD activity contributes to the balance of cell wall flexibility and strength facilitating expansion of the cell tip and, together with actin, the nascent cell plate.

Division of labor of CESA and CSLDs

Localization of both CESAs and CSLDs in cell plates and root hairs (Fujita and Wasteneys, 2014; Gu et al., 2016; Miart et al., 2014) suggests that these β-1,4-glucan synthases both contribute to cytokinesis and tip growth. Functional differentiation between CESAs and CSLDs could include differences in the properties of the cellulose fibrils produced and CSC guidance mechanism. Movement in the plasma membrane (Fig. 5) along with the formation of oligomers in vitro (Yang et al., 2020) indicate that CSLDs function in complexes, but the nature of the CSLD complexes and the microfibrils they produce is unknown. Growing tips and cell plates may have special biophysical requirements that are met by CSLDs synthesizing fibrils that differ from CESA-produced fibrils in their mechanical properties. Microfibrils have been imaged in cell plates (Fujita and Wasteneys, 2014) and in root hair tips (Mulder et al., 2004). In both cases, the microfibrils were similar in dimensions, but less ordered than microfibrils in mature cell walls. This may mean that CESAs and CSLDs synthesize similar microfibrils. Alternatively, the microfibrils could be synthesized by CESAs present during the later stages of cell plate formation (Miart et al., 2014) and by widely spaced CESAs in root hair tips (Mulder et al., 2004). CESA movement is known to track along microtubules (Paredez et al., 2006). In contrast, we have shown that CSLD trajectories are independent of microtubule orientation in *P. patens* protonemata (Fig. 6), providing a plausible explanation for the deposition of disordered microfibrils in cell plates and the apical regions of tip growing cells if they are synthesized by CSLDs. In vivo characterization of CSLD complexes and the microfibrils they synthesize will be required to distinguish among these alternatives.

Materials and methods

Vector construction

All primer pairs are shown in Table S2, along with annealing temperatures used for PCR. Amplification with Taq Polymerase (New England Biolabs) included a 3-min denaturation at 94°C; 35 cycles of 15 s at 94°C, 30 s at the annealing temperature, and 1 min/kbp at 72°C. Amplification with Phusion Polymerase (New England Biolabs) included a 30-s denaturation at 98°C; 35 cycles of 7 s at 98°C, 7 s at the annealing temperature, and 30 s/kbp at 72°C.

The CSLD2KO and CSLD6KO vectors were constructed using Gateway Multisite Pro cloning (Invitrogen) as described previously (Roberts et al., 2011). Flanking sequences 5′ and-3′ of the coding regions were amplified with appropriate primer pairs (Table S2) using Phusion DNA polymerase (New England Biolabs) and cloned into pDONR 221 P1-P4 and pDONR 221 P3-P2, respectively, using BP Clonase II (Invitrogen). The *hph* selection cassette was amplified from BHNSR (gift of Didier Schaefer, University of Neuchâtel, Neuchâtel, Switzerland) and cloned into pDONR 221 P3r-P4r. All entry clones were sequence verified. Entry clones with *CSLD2* and *CSLD6* flanking sequences in pDONR 221 P1-P4 and pDONR 221 P3-P2 were linked with the entry clone containing the *hph* selection cassette or an *nph* selection cassette (Norris et al., 2017), respectively, and inserted into pGEM-gate (Vidali et al., 2009b) using LR Clonase II Plus (Invitrogen). The resulting plasmids were cut with BsrGI for transformation into *P. patens*.

Expression vectors for HA-tagged PpCSLDs under control of their native promoters were constructed using Gateway Multisite Pro cloning (Invitrogen). The *CSLD2* and *CSLD6* coding sequences were amplified from cDNA clones pdp04669 and pdp21814 (RIKEN BioResource Center), respectively, using Phusion DNA polymerase (New England Biolabs) with forward primers containing a single hemagglutinin (HA) tag and appropriate reverse primers (Table S2), and cloned into pDONR 221 P5-P2 using BP Clonase II (Invitrogen). Similarly, the *CSLD2* and *CSLD6* promoters (~2 Kb upstream of the start codons) were amplified from *P. patens* genomic DNA and cloned into pDONR 221 P1-P5r. All entry clones were sequence verified. Promoter entry clones were linked to entry clones containing their respective *HA-PpCSLD* coding sequences and inserted into pSi3(TH)GW (Tran and Roberts, 2016) using LR Clonase II Plus

(Invitrogen). These vectors target the expression cassettes to the intergenic 108 locus, which can be disrupted with no effect on phenotype (Schaefer and Zrÿd, 1997). Rescue vectors were cut with SwaI for transformation into a *P. patens csld2/6*KO lines from which the *hph* resistance cassette had been removed (see below).

CRISPR-mediated homology directed repair was used to insert sequences encoding fluorescent proteins in frame with each *CSLD* gene and to generate the TEN mutant in *CSLD6*. To clone the protospacer(s) near the ATG (Figure S3, A and B), we generated a modified version of pMH-Cas9-gate (Mallett et al., 2019). In this modified vector, the Gateway cassette was replaced with the PpU6 promoter followed by two unique restriction sites (PmeI and SnaBI) and the *S. pyogenes* scaffold RNA sequence from pENTR-PpU6p-sgRNA-L1L2 (Mallett et al., 2019), generating pMH-Cas9. For *CSLD6*, two single-stranded oligos (Table S2) containing the protospacer sequences and sequences that overlap with pMH-Cas9 were assembled into pMH-Cas9 using Hi-Fi DNA Assembly Mastermix (NEB). For all other CSLD genes, a single protospacer (Table S2) was used. The Hi-Fi reaction was transformed into *E. coli* and used directly to inoculate a 50 ml culture. For *CSLD6*, a midi prep isolated a mix of pMH-Cas9-PS1 and pMH-Cas9-PS2 plasmids, and this mixture was used to transform moss. For all other CSLDs, a midi prep for each CRISPR plasmid was isolated individually and then transformed into moss. The homology plasmids were assembled using Hi-Fi DNA Assembly Mastermix (NEB) with four PCR-generated DNA fragments (see Table S2 for primers): ~800 bp flanking sequences 5′ and-3′ of the start codon, sequences of mEGFP or mScarlet-I, and the pGEM vector. To generate the TEN mutant, double stranded oligos (Table S2) were used as a homology template. To insert mEGFP in-frame with the CESA10 gene, the CRISPR-Cas9 vector was constructed as described previously (Mallett et al., 2019). A protospacer targeting a site near the *CESA10* start codon (Table S2) was annealed as described previously (Mallett et al., 2019) and ligated into the pENTR-Ppu6p-sgRNA-L1L2 entry vector using Golden Gate assembly (New England Biolabs) in a 10 µl reaction containing 19 fmoles of entry vector and 55 fmoles of annealed protospacer incubated at 37°C for 1 h and 60°C for 5 min. The entry vector was cloned into pMK-Cas9-gate conferring G-418 resistance using LR Clonase II Plus according to the manufacturer's instructions (Invitrogen). All plasmids were sequence verified. We used a homology repair plasmid originally designed for homologous recombination. An entry clone encoding an mEGFP-CESA10 translational fusion in pDONR 221 P5-P2 was constructed by PCR fusion of the *mEGFP* coding sequence amplified from an expression clone containing a pDONR 221 P1-P5r mEGFP entry clone and the *CESA10* coding sequence amplified from expression clone 3X*HA-CESA10* in xt18 using the appropriate primers (Table S2) as described previously (Scavuzzo-Duggan et al., 2015). The entry clone was inserted into pSi3(TH)GW along with the pDONR 221 P1-P5r entry clone containing the *PpCESA10* promoter (Tran and Roberts, 2016).

Culture and transformation of *P. patens*

Wild-type *P. patens* lines (haploid) derived from the sequenced Gransden strain (Rensing et al., 2008) by selfing and propagation from a single spore in 2011 (GD11) was a gift of Pierre-Francois Perroud, Marburg University. Wild-type and transformed *P. patens* lines were cultured on basal medium supplemented with ammonium tartrate (BCDAT) as described previously (Roberts et al., 2011). Protoplasts were prepared and transformed as described previously (Roberts et al., 2011). Stable transformants were selected with 50 µg ml^{-1} G418 (CSLD6KO; vector) or 15 µg ml^{-1} hygromycin (CSLD2KO and complementation vectors). The *hph* selection cassette was removed from *csld2/6*KO as described previously (Norris et al., 2017). CRISPR-Cas9 transformation and selection methods were described previously (Mallett et al., 2019). Tagging was performed by co-transforming the CRISPR plasmid(s) containing the protospacer sequence and the homology plasmid.

Analysis of knockout lines

For PCR analysis of target integration, target-gene disruption, and selection cassette excision, DNA was extracted as described previously (Roberts et al., 2011) and amplified using primers listed in Table S2. Sanger sequencing was employed to sequence PCR products. Plant area was analyzed as described previously (Bibeau and Vidali, 2014; Li et al., 2019; Vidali et al., 2007).

Laser scanning confocal and variable angle epifluorescence microscopy

To image mEGFP/mScarlet-CSLD6 localization and dynamics, we employed two sample preparation methods. For long-term imaging (>2 h), we used microfluidic imaging chambers (Bascom et al., 2016). Ground protonemal tissue was gently pipetted into the central part of the device followed by an infusion of Hoagland's medium. Then the chamber was submerged in Hoagland's medium (4 mM KNO_3, 2 mM KH_2PO_4, 1 mM $Ca(NO_3)_2$, 89 µM Fe citrate, 300 µM $MgSO_4$, 9.93 µM H_3BO_3, 220 nM $CuSO_4$, 1.966 µM $MnCl_2$, 231 nM $CoCl_2$, 191 nM $ZnSO_4$, 169 nM KI, 103 nM Na_2MoO_4), and placed under constant 85 µmol photons $m^{-2}s$ $light^{-1}$. For short-term imaging (<2 h), 5- to 8-d-old plants regenerated from protoplasts were placed onto an agar pad in Hoagland's medium, covered by a glass coverslip and sealed with VALAP (1:1:1 parts of Vaseline, lanoline, and paraffin). For inhibitors, the desired concentration of each inhibitor was added to the Hoagland's solution that was directly applied onto agar pad. For untreated control samples, Hoagland's solution without any inhibitor was used. Inhibitor concentrations used in this paper: Latrunculin B; 5 mM stock solution in DMSO and 25 µM in Hoagland's solution in agar pad. DCB; 40 mM stock solution in EtOH and 10 µM in Hoagland's solution in agar pad. Isoxaben; 40 mM stock solution in EtOH and 10 µM in Hoagland's solution in agar pad. For aniline blue staining, aniline blue stock solution (0.1% in 0.01 M K_2HPO_4pH12) was diluted to 0.025% in Hoagland's solution and added to the agar pad before imaging.

For confocal microscopy, images were acquired on a Nikon A1R confocal microscope system with either a 0.75. NA 20X air objective (Nikon; gametophore images) or a 1.49 NA 60X oil immersion objective (Nikon; protonemata images) at room temperature. Image acquisition was controlled by NIS-Element AR 4.1 software (Nikon). Laser illumination at 405 nm was used to excite aniline blue (laser power, 1–1.5%; Gain, 40–60; PMT

offset, 28–33); 488 nm for mEGFP (laser power, 0.5–1%; Gain, 40–60; PMT offset, 28–33); 561 nm for mScarlet (laser power, 0.5–1%; Gain, 40–60; PMT offset, 28–33). Emission filters were 525/50 nm for aniline blue and mEGFP; 595/50 nm for mScarlet. Both channels were equipped with GaAsP PMTs. Sequential acquisition was used whenever imaging aniline blue and mEGFP.

For VAEM, images were acquired with a Nikon Ti-E inverted microscope equipped with a TI-TIRF-PAU illuminator, using a Nikon 1.49 NA 100× oil immersion TIRF objective. The 1.5× optivar was used for all images to increase magnification. mEGFP and mCherry were illuminated with 488 and 561 nm laser, respectively. The laser illumination angle was adjusted individually for each sample to achieve the maximum signal-to-noise ratio. Signals for each channel were captured simultaneously with a dual-view adaptor (Photometrics) and an Andor 897 EMCCD camera. Emission filters were 525/50 nm for GFP and 595/50 for mCherry. Image acquisition was controlled by Nikon NIS-Elements software. All data were processed with enhanced contrast (0.1% pixel saturation), subtract background (rolling ball radius 20–30), and smoothing in Fiji.

Particle tracking

mEGFP-CesA10 and mEGFP-CSLD6 particles were imaged with VAEM every 2 s for 10–20 min. Images were processed before tracking using subtract background and enhance contrast in Fiji. Particle tracking was performed with the Fiji plugin TrackMate (Tinevez et al., 2017). For CesA10, stacks were reduced by 15, resulting in 30 s time intervals between frames. For CSLD6, stacks were reduced by 6, resulting in 12 s time intervals between frames. LoG detector (estimate blob diameter 0.3 µm) and LAP tracker (frame to frame linking max distance 0.5 µm; Penalties: Quality = 1; no gap closing allowed) were selected. The filters on tracks were set as follows: duration >60 s; track displacement >0.5 µm. For CesA10, tracks with track mean speed > 0.012 were excluded. Mean speed and the confinement ratio of tracks were obtained and plotted in Fig. 5. The confinement ratio is a ratio of the straight-line distance between the start and end point of the trajectory divided by the actual trajectory distance. The closer the confinement ratio value is to one, the more linear the trajectory.

Phylogenetic analysis

For phylogenetic analysis, we included *P. patens CSLD* sequences identified previously (Roberts and Bushoven, 2007) along with sequences identified previously in the conifer *Picea abies* (Yin et al., 2014), the lycophyte *Selaginella moellendorffii* (Harholt et al., 2012), and the charophyte green alga *Coleochaete orbicularis* (Mikkelsen et al., 2014) and identified by BLAST in the genome of the liverwort *Marchantia polymorpha* (Bowman et al., 2017). We included CSLDs from angiosperm species in which CSLD function has been investigated, including *Arabidopsis thaliana* (Richmond and Somerville, 2000), *Gossypium raimondii* (Li et al., 2017), *Populus trichocarpa*, *Zea mays*, and *Oryza sativa* (Yin et al., 2014). Sequences were aligned using Clustal/W with BLOSUM cost matrix, gap open cost of 10, and gap extension cost of 0.1. The alignments were edited to remove gaps and adjacent poorly aligned segments (Baldauf, 2003) and rapid bootstrapping (1,000 replicates) and search for the best-scoring maximum likelihood tree was carried out using RAxML 7.2.8, GAMMA BLOSUM62 protein model. The tree was exported from Geneious 8.1 and edited with Inkscape (https://inkscape.org/en/).

Accession numbers

P. patens CSLD names and sequence IDs are summarized in Table S3. Other sequence data from this article can be found in the GenBank/Phytozome data libraries under accession numbers included in Fig. 1.

Statistical analysis

Statistical analyses were performed with Kaleidagraph Version 5.0 (Synergy Software). The Kruskal–Wallis non-parametric test was used for pairwise comparisons in Fig. 5, C and E. ANOVA for multiple comparisons using the Tukey HSD post hoc tests was used in Fig. S2 D.

Online supplemental material

Fig. S1 shows synteny and expression analysis of *P. patens CSLD* genes. An alignment of CSLD6 and CESA10 protein sequences is shown to indicate key sequence features. Fig. S2 shows molecular and phenotypic characterization of knock out lines. Fig. S3 shows molecular characterization of tagged *CSLD* loci, complementation of mScarlet-CSLD6, and localization of the mEGFP-CSLD6. Fig. S4 shows molecular characterization of the tagged *CESA10* locus and the TEN *CSLD6* mutant. Fig. S5 shows that treatment of protonemal cells with isoxaben and isoxaben + LatB does not affect cell plate formation. Table S1 lists the lines generated in this study, which are available upon request. Table S2 lists the primer sequences used to generate constructs, mutant lines, and for genotyping. Table S3 lists the accession numbers for the *CSLD* genes. Video 1 shows mScarlet-CSLD6 localization in gametophores. Video 2 shows mScarlet-CSLD6 and lifeact-mEGFP localization in a protonemal filament. Video 3 shows mScarlet-CSLD6 and lifeact-mEGFP localization in an emerging and dividing branching protonemal cell. Video 4 shows mScarlet-CSLD6 and lifeact-mEGFP localization in a dividing apical protonemal cell. Video 5 shows VAEM imaging of GFP-CesA10, mEGFP-CLSD6, and mEGFP-CSLD6-TEN under control conditions, as well as mEGFP-CSLD6 treated with isoxaben or DCB. Video 6 shows mScarlet-CSLD6 in apical protonemal cells under control conditions and treated with 20 µM isoxaben or 10 µM DCB. Video 7 shows simultaneous VAEM imaging of mScarlet-CSLD6 and GFP-tubulin in a protonemal cell. Video 8 shows mScarlet-CSLD6 behavior during cell division in an apical protonemal cell under control conditions and treated with 10 µM DCB. Video 9 shows mScarlet-CSLD6 behavior during cell division in an apical protonemal cell treated with 25 µM LatB. Video 10 shows mScarlet-CSLD6 behavior during cell division in an apical protonemal cell treated with 10 µM DCB and 25 µM LatB.

Data availability

Tracking data underlying Fig. 5 is available on the Dryad data repository (https://doi.org/10.5061/dryad.kwh70rz8m). All other data are available in the article.

Acknowledgments

This work was supported by a grant from the National Science Foundation to A.W. Roberts (IOS-2124176) and to M. Bezanilla (IOS-2124178). Additional support was provided by University of Rhode Island Division of Research and Economic Development Bridge Grant to A.W. Roberts (construction and characterization of csld knockout lines) and as part of The Center for LignoCellulose Structure and Formation, an Energy Frontier Research Center funded by the U.S. Department of Energy, Office of Science, Basic Energy Sciences under Award #DE-SC0001090 (construction and characterization of FP-CESA10). Some material is based upon work conducted at a Rhode Island NSF EPSCoR research facility, the Genomics and Sequencing Center, supported in part by the National Science Foundation EPSCoR Cooperative Agreement #EPS-1004057.

Author contributions: A.W. Roberts, M. Bezanilla, and S.-Z. Wu designed the research; S.-Z. Wu, A.M. Chaves, R. Li, A.W. Roberts, and M. Bezanilla performed research and analyzed data; A.W. Roberts and M. Bezanilla wrote the paper.

Disclosures: The authors declare no competing interests exist.

Submitted: 21 December 2022
Revised: 28 February 2023
Accepted: 17 March 2023

References

Anderson, C.T., and J.J. Kieber. 2020. Dynamic construction, perception, and remodeling of plant cell walls. *Annu. Rev. Plant Biol.* 71:39–69. https://doi.org/10.1146/annurev-arplant-081519-03584

Baldauf, S.L. 2003. Phylogeny for the faint of heart: A tutorial. *Trends Genet.* 19:345–351. https://doi.org/10.1016/S0168-9525(03)00112-4

Bascom, C.S., Jr, L.J. Winship, and M. Bezanilla. 2018. Simultaneous imaging and functional studies reveal a tight correlation between calcium and actin networks. *Proc. Natl. Acad. Sci. USA.* 115:E2869–E2878. https://doi.org/10.1073/pnas.1711037115

Bascom, C.S., Jr, S.Z. Wu, K. Nelson, J. Oakey, and M. Bezanilla. 2016. Long-term growth of moss in microfluidic devices enables subcellular studies in development. *Plant Physiol.* 172:28–37. https://doi.org/10.1104/pp.16.00879

Bernal, A.J., J.K. Jensen, J. Harholt, S. Sørensen, I. Moller, C. Blaukopf, B. Johansen, R. de Lotto, M. Pauly, H.V. Scheller, and W.G. Willats. 2007. Disruption of ATCSLD5 results in reduced growth, reduced xylan and homogalacturonan synthase activity and altered xylan occurrence in Arabidopsis. *Plant J.* 52:791–802. https://doi.org/10.1111/j.1365-313X.2007.03281.x

Bernal, A.J., C.M. Yoo, M. Mutwil, J.K. Jensen, G. Hou, C. Blaukopf, I. Sørensen, E.B. Blancaflor, H.V. Scheller, and W.G. Willats. 2008. Functional analysis of the cellulose synthase-like genes CSLD1, CSLD2, and CSLD4 in tip-growing Arabidopsis cells. *Plant Physiol.* 148:1238–1253. https://doi.org/10.1104/pp.108.121939

Berry, E.A., M.L. Tran, C.S. Dimos, M.J. Budziszek Jr, T.R. Scavuzzo-Duggan, and A.W. Roberts. 2016. Immuno and affinity cytochemical analysis of cell wall composition in the moss Physcomitrella patens. *Front. Plant Sci.* 7:248. https://doi.org/10.3389/fpls.2016.00248

Bibeau, J.P., F. Furt, S.I. Mousavi, J.L. Kingsley, M.F. Levine, E. Tüzel, and L. Vidali. 2020. In vivo interactions between myosin XI, vesicles and filamentous actin are fast and transient in Physcomitrella patens. *J. Cell Sci.* 133:234682. https://doi.org/10.1242/jcs.234682

Bibeau, J.P., and L. Vidali. 2014. Morphological analysis of cell growth mutants in Physcomitrella. *Methods Mol. Biol.* 1080:201–213. https://doi.org/10.1007/978-1-62703-643-6_17

Bidhendi, A.J., and A. Geitmann. 2016. Relating the mechanics of the primary plant cell wall to morphogenesis. *J. Exp. Bot.* 67:449–461. https://doi.org/10.1093/jxb/erv535

Bindels, D.S., L. Haarbosch, L. van Weeren, M. Postma, K.E. Wiese, M. Mastop, S. Aumonier, G. Gotthard, A. Royant, M.A. Hink, and T.W. Gadella Jr. 2017. mScarlet: A bright monomeric red fluorescent protein for cellular imaging. *Nat. Methods.* 14:53–56. https://doi.org/10.1038/nmeth.4074

Bowman, J.L., T. Kohchi, K.T. Yamato, J. Jenkins, S. Shu, K. Ishizaki, S. Yamaoka, R. Nishihama, Y. Nakamura, F. Berger, et al. 2017. Insights into land plant evolution garnered from the Marchantia polymorpha genome. *Cell.* 171:287–304.e15. https://doi.org/10.1016/j.cell.2017.09.030

Brown, R.M., Jr., 1996. The biosynthesis of cellulose. *J. Macromol. Sci. Part A Pure Appl. Chem.* 10:1345–1373. https://doi.org/10.1080/10601329608014912

Brown, R.M., Jr, and D. Montezinos. 1976. Cellulose microfibrils: Visualization of biosynthetic and orienting complexes in association with the plasma membrane. *Proc. Natl. Acad. Sci. USA.* 73:143–147. https://doi.org/10.1073/pnas.73.1.143

DeBolt, S., R. Gutierrez, D.W. Ehrhardt, and C. Somerville. 2007. Nonmotile cellulose synthase subunits repeatedly accumulate within localized regions at the plasma membrane in Arabidopsis hypocotyl cells following 2,6-dichlorobenzonitrile treatment. *Plant Physiol.* 145:334–338. https://doi.org/10.1104/pp.107.104703

Diotallevi, F., and B. Mulder. 2007. The cellulose synthase complex: A polymerization driven supramolecular motor. *Biophys. J.* 92:2666–2673. https://doi.org/10.1529/biophysj.106.099473

Doblin, M.S., L. De Melis, E. Newbigin, A. Bacic, and S.M. Read. 2001. Pollen tubes of Nicotiana alata express two genes from different beta-glucan synthase families. *Plant Physiol.* 125:2040–2052. https://doi.org/10.1104/pp.125.4.2040

Emons, A.M.C. 1994. Winding threads around plant cells: A geometrical model for microfibril deposition. *Plant Cell Environ.* 17:3–14. https://doi.org/10.1111/j.1365-3040.1994.tb00261.x

Favery, B., E. Ryan, J. Foreman, P. Linstead, K. Boudonck, M. Steer, P. Shaw, and L. Dolan. 2001. KOJAK encodes a cellulose synthase-like protein required for root hair cell morphogenesis in Arabidopsis. *Genes Dev.* 15:79–89. https://doi.org/10.1101/gad.188801

Fernandez-Pozo, N., F.B. Haas, R. Meyberg, K.K. Ullrich, M. Hiss, P.F. Perroud, S. Hanke, V. Kratz, A.F. Powell, E.F. Vesty, et al. 2020. PEATmoss (Physcomitrella expression atlas tool): A unified gene expression atlas for the model plant Physcomitrella patens. *Plant J.* 102:165–177. https://doi.org/10.1111/tpj.14607

Fujita, M., and G.O. Wasteneys. 2014. A survey of cellulose microfibril patterns in dividing, expanding, and differentiating cells of Arabidopsis thaliana. *Protoplasma.* 251:687–698. https://doi.org/10.1007/s00709-013-0571-2

Galway, M.E., R.C. Eng, J.W. Schiefelbein, and G.O. Wasteneys. 2011. Root hair-specific disruption of cellulose and xyloglucan in AtCSLD3 mutants, and factors affecting the post-rupture resumption of mutant root hair growth. *Planta.* 233:985–999. https://doi.org/10.1007/s00425-011-1355-6

Goss, C.A., D.J. Brockmann, J.T. Bushoven, and A.W. Roberts. 2012. A CELLULOSE SYNTHASE (CESA) gene essential for gametophore morphogenesis in the moss Physcomitrella patens. *Planta.* 235:1355–1367. https://doi.org/10.1007/s00425-011-1579-5

Gu, F., M. Bringmann, J.R. Combs, J. Yang, D.C. Bergmann, and E. Nielsen. 2016. Arabidopsis CSLD5 functions in cell plate formation in a cell cycle-dependent manner. *Plant Cell.* 28:1722–1737. https://doi.org/10.1105/tpc.16.00203

Gu, F., and E. Nielsen. 2013. Targeting and regulation of cell wall synthesis during tip growth in plants. *J. Integr. Plant Biol.* 55:835–846. https://doi.org/10.1111/jipb.12077

Gu, Y., and C.G. Rasmussen. 2022. Cell biology of primary cell wall synthesis in plants. *Plant Cell.* 34:103–128. https://doi.org/10.1093/plcell/koab249

Hamant, O., and E.S. Haswell. 2017. Life behind the wall: Sensing mechanical cues in plants. *BMC Biol.* 15:59. https://doi.org/10.1186/s12915-017-0403-5

Harholt, J., I. Sørensen, J. Fangel, A. Roberts, W.G.T. Willats, H.V. Scheller, B.L. Petersen, J.A. Banks, and P. Ulvskov. 2012. The glycosyltransferase repertoire of the spikemoss Selaginella moellendorffii and a comparative study of its cell wall. *PLoS One.* 7:e35846. https://doi.org/10.1371/journal.pone.0035846

Herth, W. 1980. Calcofluor white and Congo red inhibit chitin microfibril assembly of Poterioochromonas: Evidence for a gap between polymerization and microfibril formation. *J. Cell Biol.* 87:442–450. https://doi.org/10.1083/jcb.87.2.442

Hiss, M., O. Laule, R.M. Meskauskiene, M.A. Arif, E.L. Decker, A. Erxleben, W. Frank, S.T. Hanke, D. Lang, A. Martin, et al. 2014. Large-scale gene

expression profiling data for the model moss Physcomitrella patens aid understanding of developmental progression, culture and stress conditions. *Plant J.* 79:530–539. https://doi.org/10.1111/tpj.12572

Hu, H., R. Zhang, S. Dong, Y. Li, C. Fan, Y. Wang, T. Xia, P. Chen, L. Wang, S. Feng, et al. 2018. AtCSLD3 and GhCSLD3 mediate root growth and cell elongation downstream of the ethylene response pathway in Arabidopsis. *J. Exp. Bot.* 69:1065–1080. https://doi.org/10.1093/jxb/erx470

Hu, H., R. Zhang, Y. Tang, C. Peng, L. Wu, S. Feng, P. Chen, Y. Wang, X. Du, and L. Peng. 2019. Cotton CSLD3 restores cell elongation and cell wall integrity mainly by enhancing primary cellulose production in the Arabidopsis cesa6 mutant. *Plant Mol. Biol.* 101:389–401. https://doi.org/10.1007/s11103-019-00910-1

Hu, J., L. Zhu, D. Zeng, Z. Gao, L. Guo, Y. Fang, G. Zhang, G. Dong, M. Yan, J. Liu, and Q. Qian. 2010. Identification and characterization of NARROW AND ROLLED LEAF 1, a novel gene regulating leaf morphology and plant architecture in rice. *Plant Mol. Biol.* 73:283–292. https://doi.org/10.1007/s11103-010-9614-7

Hunter, C.T., D.H. Kirienko, A.W. Sylvester, G.F. Peter, D.R. McCarty, and K.E. Koch. 2012. Cellulose Synthase-Like D1 is integral to normal cell division, expansion, and leaf development in maize. *Plant Physiol.* 158:708–724. https://doi.org/10.1104/pp.111.188466

Jarvis, M.C. 2018. Structure of native cellulose microfibrils, the starting point for nanocellulose manufacture. *Phil Trans R Soc A. Math Phys Eng Sci.* 376:20170045. https://doi.org/10.1098/rsta.2017.0045

Karas, B.J., L. Ross, M. Novero, L. Amyot, A. Shrestha, S. Inada, M. Nakano, T. Sakai, D. Bonetta, S. Sato, et al. 2021. Intragenic complementation at the Lotus japonicus CELLULOSE SYNTHASE-LIKE D1 locus rescues root hair defects. *Plant Physiol.* 186:2037–2050. https://doi.org/10.1093/plphys/kiab204

Kim, C.M., S.H. Park, B.I. Je, S.H. Park, S.J. Park, H.L. Piao, M.Y. Eun, L. Dolan, and C.D. Han. 2007. OsCSLD1, a cellulose synthase-like D1 gene, is required for root hair morphogenesis in rice. *Plant Physiol.* 143:1220–1230. https://doi.org/10.1104/pp.106.091546

Kimura, S., W. Laosinchai, T. Itoh, X. Cui, C.R. Linder, and R.M. Brown Jr. 1999. Immunogold labeling of rosette terminal cellulose-synthesizing complexes in the vascular plant vigna angularis. *Plant Cell.* 11:2075–2086. https://doi.org/10.1105/tpc.11.11.2075

Kubicki, J.D., H. Yang, D. Sawada, H. O'Neill, D. Oehme, and D. Cosgrove. 2018. The shape of native plant cellulose microfibrils. *Sci. Rep.* 8:13983. https://doi.org/10.1038/s41598-018-32211-w

Lang, D., K.K. Ullrich, F. Murat, J. Fuchs, J. Jenkins, F.B. Haas, M. Piednoel, H. Gundlach, M. Van Bel, R. Meyberg, et al. 2018. The Physcomitrella patens chromosome-scale assembly reveals moss genome structure and evolution. *Plant J.* 93:515–533. https://doi.org/10.1111/tpj.13801

Larson, R.T., and H.E. McFarlane. 2021. Small but mighty: An update on small molecule plant cellulose biosynthesis inhibitors. *Plant Cell Physiol.* 62:1828–1838. https://doi.org/10.1093/pcp/pcab108

Li, L., S. Hey, S. Liu, Q. Liu, C. McNinch, H.C. Hu, T.J. Wen, C. Marcon, A. Paschold, W. Bruce, et al. 2016. Characterization of maize roothairless6 which encodes a D-type cellulose synthase and controls the switch from bulge formation to tip growth. *Sci. Rep.* 6:34395. https://doi.org/10.1038/srep34395

Li, M., G. Xiong, R. Li, J. Cui, D. Tang, B. Zhang, M. Pauly, Z. Cheng, and Y. Zhou. 2009. Rice cellulose synthase-like D4 is essential for normal cell-wall biosynthesis and plant growth. *Plant J.* 60:1055–1069. https://doi.org/10.1111/j.1365-313X.2009.04022.x

Li, X., T.L. Speicher, D.C.T. Dees, N. Mansoori, J.B. McManus, M. Tien, L.M. Trindade, I.S. Wallace, and A.W. Roberts. 2019. Convergent evolution of hetero-oligomeric cellulose synthesis complexes in mosses and seed plants. *Plant J.* 99:862–876. https://doi.org/10.1111/tpj.14366

Li, Y., T. Yang, D. Dai, Y. Hu, X. Guo, and H. Guo. 2017. Evolution, gene expression profiling and 3D modeling of CSLD proteins in cotton. *BMC Plant Biol.* 17:119. https://doi.org/10.1186/s12870-017-1063-x

Lindeboom, J., B.M. Mulder, J.W. Vos, T. Ketelaar, and A.M. Emons. 2008. Cellulose microfibril deposition: Coordinated activity at the plant plasma membrane. *J. Microsc.* 231:192–200. https://doi.org/10.1111/j.1365-2818.2008.02035.x

Lopez-Obando, M., B. Hoffmann, C. Géry, A. Guyon-Debast, E. Téoulé, C. Rameau, S. Bonhomme, and F. Nogué. 2016. Simple and efficient targeting of multiple genes through CRISPR-Cas9 in Physcomitrella patens. *G3.* 6:3647–3653. https://doi.org/10.1534/g3.116.033266

Luan, W., Y. Liu, F. Zhang, Y. Song, Z. Wang, Y. Peng, and Z. Sun. 2011. OsCD1 encodes a putative member of the cellulose synthase-like D sub-family and is essential for rice plant architecture and growth. *Plant Biotechnol. J.* 9:513–524. https://doi.org/10.1111/j.1467-7652.2010.00570.x

Mallett, D.R., M. Chang, X. Cheng, and M. Bezanilla. 2019. Efficient and modular CRISPR-Cas9 vector system for Physcomitrella patens. *Plant Direct.* 3:e00168. https://doi.org/10.1002/pld3.168

Miart, F., T. Desprez, E. Biot, H. Morin, K. Belcram, H. Höfte, M. Gonneau, and S. Vernhettes. 2014. Spatio-temporal analysis of cellulose synthesis during cell plate formation in Arabidopsis. *Plant J.* 77:71–84. https://doi.org/10.1111/tpj.12362

Mikkelsen, M.D., J. Harholt, P. Ulvskov, I.E. Johansen, J.U. Fangel, M.S. Doblin, A. Bacic, and W.G. Willats. 2014. Evidence for land plant cell wall biosynthetic mechanisms in charophyte green algae. *Ann. Bot.* 114:1217–1236. https://doi.org/10.1093/aob/mcu171

Moon, S., M.M. Oo, B. Kim, H.-J. Koh, S.A. Oh, G. Yi, G. An, S.K. Park, and K.-H. Jung. 2018. Genome-wide analyses of late pollen-preferred genes conserved in various rice cultivars and functional identification of a gene involved in the key processes of late pollen development. *Rice.* 11:28. https://doi.org/10.1186/s12284-018-0219-0

Mueller, S.C., and R.M. Brown Jr. 1980. Evidence for an intramembrane component associated with a cellulose microfibril-synthesizing complex in higher plants. *J. Cell Biol.* 84:315–326. https://doi.org/10.1083/jcb.84.2.315

Mulder, B., J. Schel, and A.M. Emons. 2004. How the geometrical model for plant cell wall formation enables the production of a random texture. *Cellulose.* 11:395–401. https://doi.org/10.1023/B:CELL.0000046419.31076.7f

Nixon, B.T., K. Mansouri, A. Singh, J. Du, J.K. Davis, J.G. Lee, E. Slabaugh, V.G. Vandavasi, H. O'Neill, E.M. Roberts, et al. 2016. Comparative structural and computational analysis supports eighteen cellulose synthases in the plant cellulose synthesis complex. *Sci. Rep.* 6:28696. https://doi.org/10.1038/srep28696

Norris, J.H., X. Li, S. Huang, A.M.L. Van de Meene, M.L. Tran, E. Killeavy, A.M. Chaves, B. Mallon, D. Mercure, H.-T. Tan, et al. 2017. Functional specialization of cellulose synthase isoforms in a moss shows parallels with seed plants. *Plant Physiol.* 175:210–222. https://doi.org/10.1104/pp.17.00885

Oehme, D.P., M.T. Downton, M.S. Doblin, J. Wagner, M.J. Gidley, and A. Bacic. 2015. Unique aspects of the structure and dynamics of elementary Iβ cellulose microfibrils revealed by computational simulations. *Plant Physiol.* 168:3–17. https://doi.org/10.1104/pp.114.254664

Ortiz-Ramírez, C., M. Hernandez-Coronado, A. Thamm, B. Catarino, M. Wang, L. Dolan, J.A. Feijó, and J.D. Becker. 2016. A transcriptome atlas of Physcomitrella patens provides insight into the evolution and development of land plants. *Mol. Plant.* 9:205–220. https://doi.org/10.1016/j.molp.2015.12.002

Pancaldi, F., E.N. van Loo, M.E. Schranz, and L.M. Trindade. 2022. Genomic architecture and evolution of the Cellulose synthase gene superfamily as revealed by phylogenomic analysis. *Front. Plant Sci.* 13:870818. https://doi.org/10.3389/fpls.2022.870818

Paredez, A.R., C.R. Somerville, and D.W. Ehrhardt. 2006. Visualization of cellulose synthase demonstrates functional association with microtubules. *Science.* 312:1491–1495. https://doi.org/10.1126/science.1126551

Park, S., A.L. Szumlanski, F. Gu, F. Guo, and E. Nielsen. 2011. A role for CSLD3 during cell-wall synthesis in apical plasma membranes of tip-growing root-hair cells. *Nat. Cell Biol.* 13:973–980. https://doi.org/10.1038/ncb2294

Pear, J.R., Y. Kawagoe, W.E. Schreckengost, D.P. Delmer, and D.M. Stalker. 1996. Higher plants contain homologs of the bacterial celA genes encoding the catalytic subunit of cellulose synthase. *Proc. Natl. Acad. Sci. USA.* 93:12637–12642. https://doi.org/10.1073/pnas.93.22.12637

Pedersen, G.B., L. Blaschek, K.E.H. Frandsen, L.C. Noack, and S. Persson. 2023. Cellulose synthesis in land plants. *Mol. Plant.* 16:206–231. https://doi.org/10.1016/j.molp.2022.12.015

Peng, X., H. Pang, M. Abbas, X. Yan, X. Dai, Y. Li, and Q. Li. 2019. Characterization of Cellulose synthase-like D (CSLD) family revealed the involvement of PtrCslD5 in root hair formation in Populus trichocarpa. *Sci. Rep.* 9:1452. https://doi.org/10.1038/s41598-018-36529-3

Penning, B.W., C.T. Hunter III, R. Tayengwa, A.L. Eveland, C.K. Dugard, A.T. Olek, W. Vermerris, K.E. Koch, D.R. McCarty, M.F. Davis, et al. 2009. Genetic resources for maize cell wall biology. *Plant Physiol.* 151:1703–1728. https://doi.org/10.1104/pp.109.136804

Perroud, P.F., F.B. Haas, M. Hiss, K.K. Ullrich, A. Alboresi, M. Amirebrahimi, K. Barry, R. Bassi, S. Bonhomme, H. Chen, et al. 2018. The Physcomitrella patens gene atlas project: Large-scale RNA-seq based expression data. *Plant J.* 95:168–182. https://doi.org/10.1111/tpj.13940

Preston, R.D. 1964. Structural and mechanical aspects of plant cell walls with particular reference to synthesis and growth. In The Formation of

Wood in Forest Trees. M.H. Zimmermann, editor. Academic Press, New York. 169–188. https://doi.org/10.1016/B978-1-4832-2931-7.50014-8
Purushotham, P., S.H. Cho, S.M. Díaz-Moreno, M. Kumar, B.T. Nixon, V. Bulone, and J. Zimmer. 2016. A single heterologously expressed plant cellulose synthase isoform is sufficient for cellulose microfibril formation in vitro. *Proc. Natl. Acad. Sci. USA*. 113:11360–11365. https://doi.org/10.1073/pnas.1606210113
Purushotham, P., R. Ho, and J. Zimmer. 2020. Architecture of a catalytically active homotrimeric plant cellulose synthase complex. *Science*. 369: 1089–1094. https://doi.org/10.1126/science.abb2978
Qi, G., R. Hu, L. Yu, G. Chai, Y. Cao, R. Zuo, Y. Kong, and G. Zhou. 2013. Two poplar cellulose synthase-like D genes, PdCSLD5 and PdCSLD6, are functionally conserved with Arabidopsis CSLD3. *J. Plant Physiol.* 170: 1267–1276. https://doi.org/10.1016/j.jplph.2013.04.014
Rensing, S.A., D. Lang, A.D. Zimmer, A. Terry, A. Salamov, H. Shapiro, T. Nishiyama, P.F. Perroud, E.A. Lindquist, Y. Kamisugi, et al. 2008. The Physcomitrella genome reveals evolutionary insights into the conquest of land by plants. *Science*. 319:64–69. https://doi.org/10.1126/science.1150646
Richmond, T.A., and C.R. Somerville. 2000. The cellulose synthase superfamily. *Plant Physiol.* 124:495–498. https://doi.org/10.1104/pp.124.2.495
Roberts, A.W., and J.T. Bushoven. 2007. The cellulose synthase (CESA) gene superfamily of the moss Physcomitrella patens. *Plant Mol. Biol.* 63: 207–219. https://doi.org/10.1007/s11103-006-9083-1
Roberts, A.W., C.S. Dimos, M.J. Budziszek Jr, C.A. Goss, and V. Lai. 2011. Knocking out the wall: Protocols for gene targeting in Physcomitrella patens. *Methods Mol. Biol.* 715:273–290. https://doi.org/10.1007/978-1-61779-008-9_19
Roberts, E., R.W. Seagull, C.H. Haigler, and R.M. Brown Jr. 1982. Alteration of cellulose microfibril formation in eukaryotic cells: Calcofluor White interferes with microfibril assembly and orientation in Oocystis apiculata. *Protoplasma*. 113:1–9. https://doi.org/10.1007/BF01283034
Rounds, C.M., and M. Bezanilla. 2013. Growth mechanisms in tip-growing plant cells. *Annu. Rev. Plant Biol.* 64:243–265. https://doi.org/10.1146/annurev-arplant-050312-120150
Samuga, A., and C.P. Joshi. 2004. Cloning and characterization of cellulose synthase-like gene, PtrCSLD2 from developing xylem of aspen trees. *Physiol. Plant.* 120:631–641. https://doi.org/10.1111/j.0031-9317.2004.0271.x
Scavuzzo-Duggan, T.R., A.M. Chaves, and A.W. Roberts. 2015. A complementation assay for in vivo protein structure/function analysis in Physcomitrella patens (Funariaceae). *Appl. Plant Sci.* 3:1500023. https://doi.org/10.3732/apps.1500023
Schaefer, D.G., and J.P. Zrÿd. 1997. Efficient gene targeting in the moss Physcomitrella patens. *Plant J.* 11:1195–1206. https://doi.org/10.1046/j.1365-313X.1997.11061195.x
Scheible, W.-R., R. Eshed, T. Richmond, D. Delmer, and C. Somerville. 2001. Modifications of cellulose synthase confer resistance to isoxaben and thiazolidinone herbicides in Arabidopsis Ixr1 mutants. *Proc. Natl. Acad. Sci. USA*. 98:10079–10084. https://doi.org/10.1073/pnas.191361598
Schumaker, K.S., and M.A. Dietrich. 1998. Hormone-induced signaling during moss development. *Annu. Rev. Plant Physiol. Plant Mol. Biol.* 49: 501–523. https://doi.org/10.1146/annurev.arplant.49.1.501
Shpigel, E., L. Roiz, R. Goren, and O. Shoseyov. 1998. Bacterial cellulose-binding domain modulates in vitro elongation of different plant cells. *Plant Physiol.* 117:1185–1194. https://doi.org/10.1104/pp.117.4.1185
Smertenko, A., F. Assaad, F. Baluška, M. Bezanilla, H. Buschmann, G. Drakakaki, M.T. Hauser, M. Janson, Y. Mineyuki, I. Moore, et al. 2017. Plant cytokinesis: Terminology for structures and processes. *Trends Cell Biol.* 27:885–894. https://doi.org/10.1016/j.tcb.2017.08.008
Tateno, M., C. Brabham, and S. DeBolt. 2016. Cellulose biosynthesis inhibitors - a multifunctional toolbox. *J. Exp. Bot.* 67:533–542. https://doi.org/10.1093/jxb/erv489
Tinevez, J.Y., N. Perry, J. Schindelin, G.M. Hoopes, G.D. Reynolds, E. Laplantine, S.Y. Bednarek, S.L. Shorte, and K.W. Eliceiri. 2017. TrackMate: An open and extensible platform for single-particle tracking. *Methods*. 115:80–90. https://doi.org/10.1016/j.ymeth.2016.09.016
Tran, M.L., T.W. McCarthy, H. Sun, S.-Z. Wu, J.H. Norris, M. Bezanilla, L. Vidali, C.T. Anderson, and A.W. Roberts. 2018. Direct observation of the effects of cellulose synthesis inhibitors using live cell imaging of Cellulose Synthase (CESA) in Physcomitrella patens. *Sci. Rep.* 8:735. https://doi.org/10.1038/s41598-017-18994-4
Tran, M.L., and A.W. Roberts. 2016. Cellulose synthase gene expression profiling of Physcomitrella patens. *Plant Biol.* 18:362–368. https://doi.org/10.1111/plb.12416
Tsekos, I. 1999. The sites of cellulose synthesis in algae: Diversity and evolution of cellulose-synthesizing enzyme complexes. *J. Phycol.* 35: 635–655. https://doi.org/10.1046/j.1529-8817.1999.3540635.x
Vandavasi, V.G., D.K. Putnam, Q. Zhang, L. Petridis, W.T. Heller, B.T. Nixon, C.H. Haigler, U. Kalluri, L. Coates, P. Langan, et al. 2016. A structural study of CESA1 catalytic domain of arabidopsis cellulose synthesis complex: Evidence for CESA trimers. *Plant Physiol.* 170:123–135. https://doi.org/10.1104/pp.15.01356
Vidali, L., R.C. Augustine, K.P. Kleinman, and M. Bezanilla. 2007. Profilin is essential for tip growth in the moss Physcomitrella patens. *Plant Cell*. 19: 3705–3722. https://doi.org/10.1105/tpc.107.053413
Vidali, L., C.M. Rounds, P.K. Hepler, and M. Bezanilla. 2009a. Lifeact-mEGFP reveals a dynamic apical F-actin network in tip growing plant cells. *PLoS One*. 4:e5744. https://doi.org/10.1371/journal.pone.0005744
Vidali, L., P.A. van Gisbergen, C. Guérin, P. Franco, M. Li, G.M. Burkart, R.C. Augustine, L. Blanchoin, and M. Bezanilla. 2009b. Rapid formin-mediated actin-filament elongation is essential for polarized plant cell growth. *Proc. Natl. Acad. Sci. USA*. 106:13341–13346. https://doi.org/10.1073/pnas.0901170106
Wang, W., L. Wang, C. Chen, G. Xiong, X.Y. Tan, K.Z. Yang, Z.C. Wang, Y. Zhou, D. Ye, and L.Q. Chen. 2011. Arabidopsis CSLD1 and CSLD4 are required for cellulose deposition and normal growth of pollen tubes. *J. Exp. Bot.* 62:5161–5177. https://doi.org/10.1093/jxb/err221
Wang, X., G. Cnops, R. Vanderhaeghen, S. De Block, M. Van Montagu, and M. Van Lijsebettens. 2001. AtCSLD3, a cellulose synthase-like gene important for root hair growth in arabidopsis. *Plant Physiol.* 126:575–586. https://doi.org/10.1104/pp.126.2.575
Wilson, T.H., M. Kumar, and S.R. Turner. 2021. The molecular basis of plant cellulose synthase complex organisation and assembly. *Biochem. Soc. Trans.* 49:379–391. https://doi.org/10.1042/BST20200697
Wolf, L., L. Rizzini, R. Stracke, R. Ulm, and S.A. Rensing. 2010. The molecular and physiological responses of Physcomitrella patens to ultraviolet-B radiation. *Plant Physiol.* 153:1123–1134. https://doi.org/10.1104/pp.110.154658
Wu, C., Y. Fu, G. Hu, H. Si, S. Cheng, and W. Liu. 2010. Isolation and characterization of a rice mutant with narrow and rolled leaves. *Planta*. 232: 313–324. https://doi.org/10.1007/s00425-010-1180-3
Wu, S.Z., and M. Bezanilla. 2018. Actin and microtubule cross talk mediates persistent polarized growth. *J. Cell Biol.* 217:3531–3544. https://doi.org/10.1083/jcb.201802039
Yang, J., G. Bak, T. Burgin, W.J. Barnes, H.B. Mayes, M.J. Peña, B.R. Urbanowicz, and E. Nielsen. 2020. Biochemical and genetic analysis identify CSLD3 as a beta-1,4-glucan synthase that functions during plant cell wall synthesis. *Plant Cell*. 32:1749–1767. https://doi.org/10.1105/tpc.19.00637
Yang, W., C. Schuster, C.T. Beahan, V. Charoensawan, A. Peaucelle, A. Bacic, M.S. Doblin, R. Wightman, and E.M. Meyerowitz. 2016. Regulation of meristem morphogenesis by cell wall synthases in Arabidopsis. *Curr. Biol.* 26:1404–1415. https://doi.org/10.1016/j.cub.2016.04.026
Yin, L., Y. Verhertbruggen, A. Oikawa, C. Manisseri, B. Knierim, L. Prak, J.K. Jensen, J.P. Knox, M. Auer, W.G. Willats, and H.V. Scheller. 2011. The cooperative activities of CSLD2, CSLD3, and CSLD5 are required for normal Arabidopsis development. *Mol. Plant*. 4:1024–1037. https://doi.org/10.1093/mp/ssr026
Yin, Y., M.A. Johns, H. Cao, and M. Rupani. 2014. A survey of plant and algal genomes and transcriptomes reveals new insights into the evolution and function of the cellulose synthase superfamily. *BMC Genomics*. 15: 260. https://doi.org/10.1186/1471-2164-15-260
Yoo, C.M., L. Quan, and E.B. Blancaflor. 2012. Divergence and redundancy in CSLD2 and CSLD3 function during Arabidopsis thaliana root hair and female gametophyte development. *Front. Plant Sci.* 3:111. https://doi.org/10.3389/fpls.2012.00111
Yoshikawa, T., M. Eiguchi, K. Hibara, J. Ito, and Y. Nagato. 2013. Rice slender leaf 1 gene encodes cellulose synthase-like D4 and is specifically expressed in M-phase cells to regulate cell proliferation. *J. Exp. Bot.* 64: 2049–2061. https://doi.org/10.1093/jxb/ert060
Zhu, J., B.H. Lee, M. Dellinger, X. Cui, C. Zhang, S. Wu, E.A. Nothnagel, and J.K. Zhu. 2010. A cellulose synthase-like protein is required for osmotic stress tolerance in Arabidopsis. *Plant J.* 63:128–140. https://doi.org/10.1111/j.1365-313X.2010.04227.x

JCB

Supplemental material

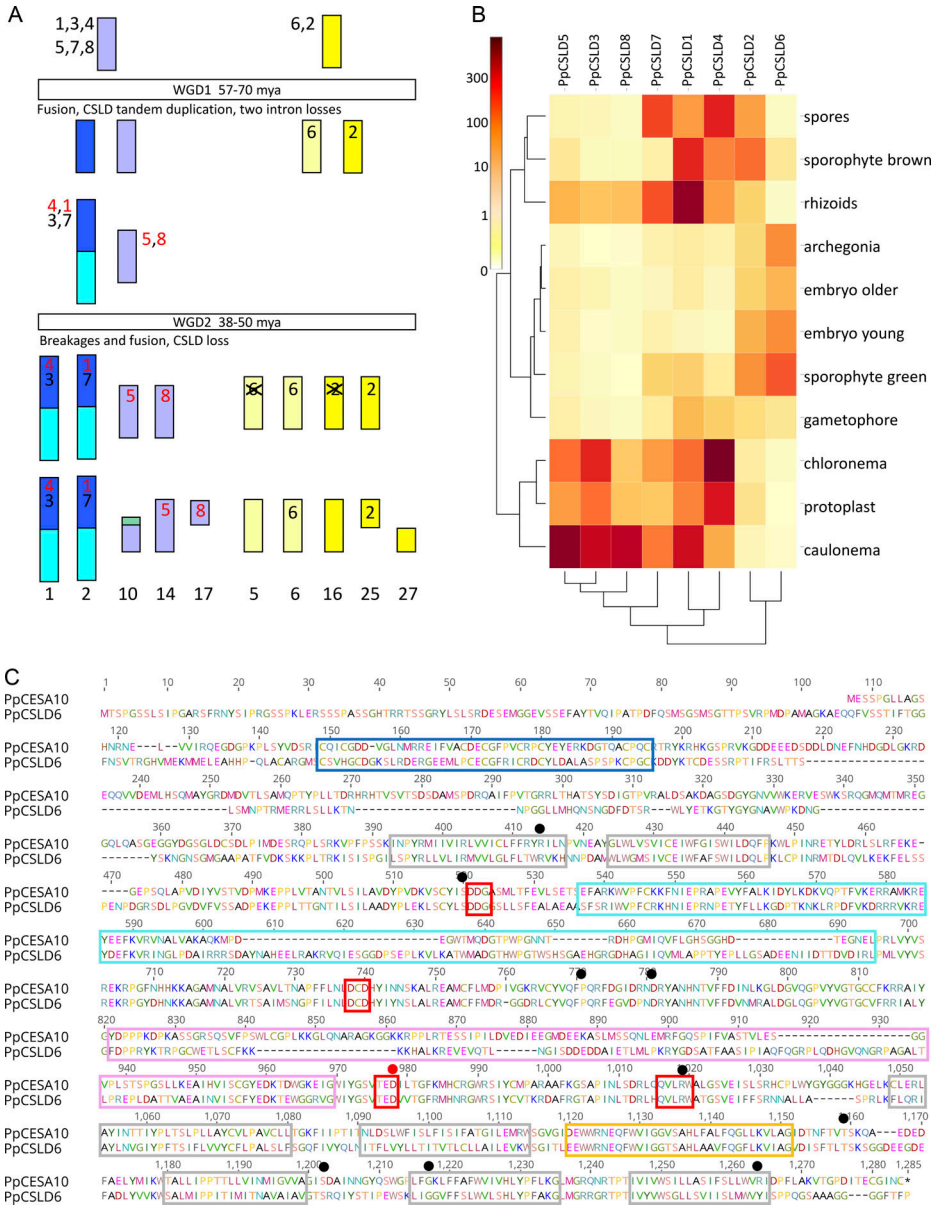

Figure S1. **Synteny, expression analysis and CSLD alignment. (A)** Synteny analysis of CSLD diversification based on the chromosome-scale assembly of the *P. patens* genome (Lang et al., 2018) shows that *CSLD2* and *CSLD6* are close paralogs. The eight *P. patens* CSLDs reside on chromosomes descended from two of the seven chromosomes proposed to have existed before the first of two whole genome duplications (WGD). *CSLD2* and *6* diverged from a common ancestor in WGD1. Following WGD2 paralogs of *CSLD6* and *CSLD2* were lost from chromosomes 5 and 16, respectively. Duplication of the chromosome carrying the common ancestor of CSD1, 3, 4, 5, 7 and 8 in WGD1 was followed by a fusion affecting the common ancestor of chromosomes 1 and 2, which both carry two *CSLD*s as tandem repeats. The tandem duplication may have occurred after WDG2 on the common ancestor of chromosomes 1 and 2 or before WGD1 followed by loss of one duplicate from the common ancestor of chromosomes 14 and 10/17. There is no evidence of loss following WGD2. Intron structure is most parsimoniously explained by intron loss. CSLD2 and 6 have three introns, the second of which is shared with *P. patens CESA*s (Roberts and Bushoven, 2007). This intron two is present in *CSLD3* and *7*, but not *CSLD1, 4, 5,* and *8* (indicated in red). Gain of intron two in CSLD2, 3, 6, and 7 is unlikely given that it is homologous with an intron in *P. patens CESA*s. It is possible that intron 2 was lost before WGD2 in the common ancestor of *CSLD5* and *8* and lost independently in the common ancestor of *CSLD1* and *4* before WGD2, but after tandem duplication of the common ancestor of *CSLD1, 3, 4,* and *7*. Alternatively, tandem duplication and loss of intron two in the common ancestor of *CSLD1, 4, 5,* and *8* may have occurred before WGD1 with loss of the paralog of the *CSLD3* and *7* common ancestor occurring before WGD2. **(B)** Transcriptional profile of *P. patens CSLD*s at different developmental stages using a NimbleGene custom microarray (Ortiz-Ramírez et al., 2016) accessed from PEATmoss (Fernandez-Pozo et al., 2020). *CSLD2* and *CSLD6* had higher expression in gametophores and sporophytes compared to protonemal tissues (chloronema and caulonema). In contrast, the other six *P. patens CSLD*s were more highly expressed in protonemal tissues and had low expression in gametophores. Results from transcriptional profiling of *P. patens* developmental stages using a CombiMatrix array (Hiss et al., 2014; Wolf et al., 2010) or RNA-seq (Perroud et al., 2018) were generally consistent, although *CSLD2* transcripts were not detected in the RNA-seq analysis. **(C)** Sequence alignment of PpCESA10 and PpCSLD with Zn-binding domain (blue), transmembrane helices (gray), plant conserved region (aqua), class-specific region (pink), interfacial helix (orange), and conserved D, D, D, QxxRW motifs (red) highlighted based on homology with PttCESA8 (Purushotham et al., 2020). The red circle indicates the location of the TEN mutation. Black circles indicate the locations of point mutations that confer isoxaben resistance in *Arabidopsis* CESAs. No DCB resistance mutation have been characterized (Larson and McFarlane, 2021).

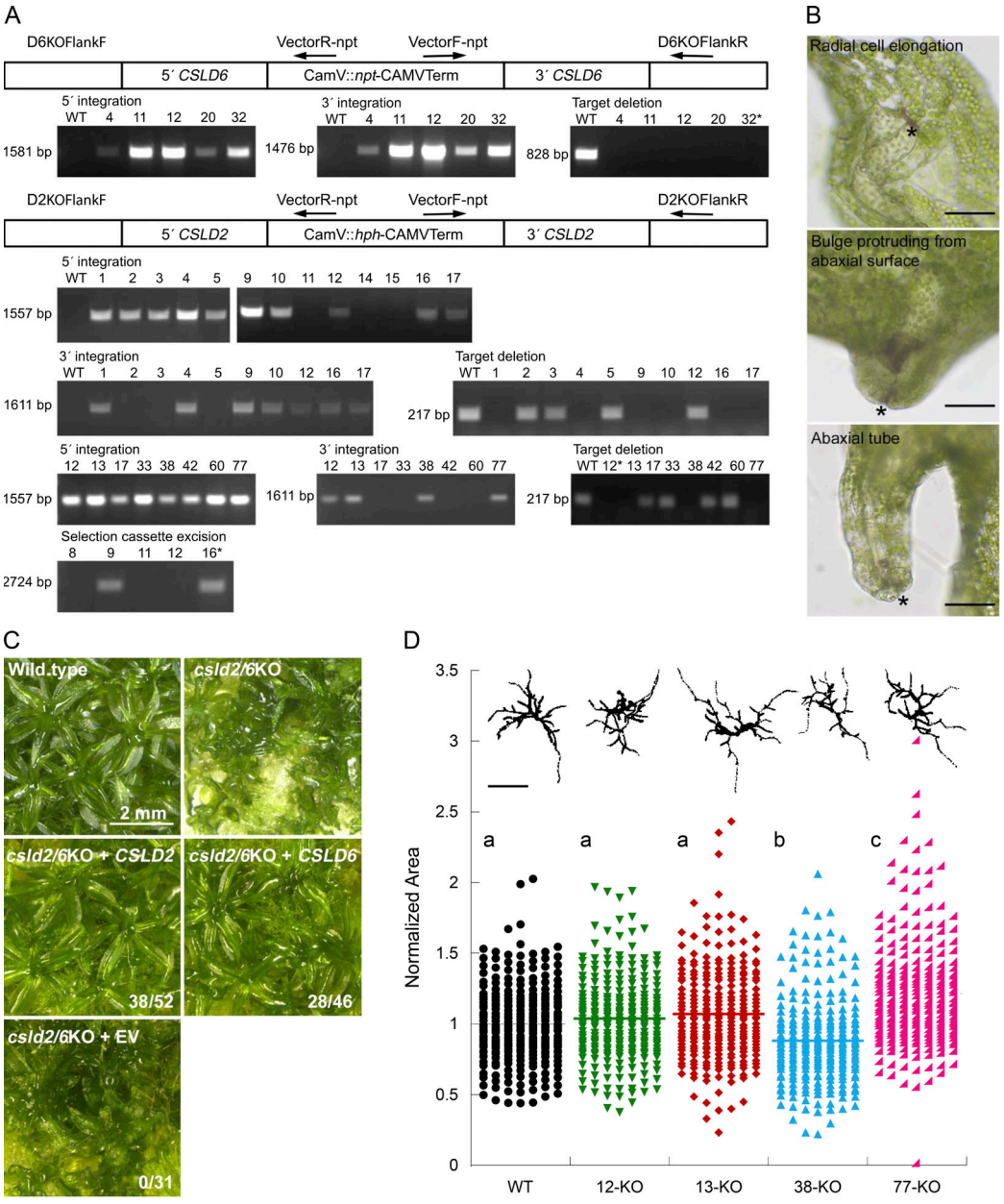

Figure S2. **Genotype and phenotype of *csld6*KO, *csld2*KO, and *csld2/6*KO. (A)** PCR-based genotyping. CSLD6KO-npt and CSLD2KO-hph vectors integrated to delete *CSLD6* and *CSLD2*, respectively, with primers used for amplification of the 5′ and-3′ integration sites (arrows). For *csld6*KO-4, -11, -12, -20 and -32 (top row), 5′ integration tested with primer pair D6KOFlankF/VectorR-npt produced the expected 1,581 bp fragment, 3′ integration tested with primer pair VectorF-npt/D6KOFlankR produced the expected 1,476 bp fragment, and target deletion was verified by the absence of a product from primers D6TargetF/D6TargetR, which anneals within the *CSLD6* coding sequence and amplified an 828 bp fragment in the wild type. For *csld2*KO (middle two rows), 5′ integration tested with primer pair D2KOFlankF/VectorR-hph produced the expected 1,557 bp fragment in 10 lines, 3′ integration tested with primer pair VectorF-hph/D2KOFlankR produced the expected 1,611 bp fragment in 7 of those lines and target deletion was verified in lines *csld2*KO-1, -4, -9, -10, -16, and -17 by the absence of a product from primers D2TargetF/D2TargetR, which anneal within the *CSLD2* coding sequence and amplify a 217 bp fragment in the wild type. For *csld2/6*KO (bottom two rows), 5′ and 3′ integration of the CSLD2KO-hph vector in *csld2*KO-32 was tested with the same primer pairs. Target deletion was verified in lines *csld2/6*KO-12, -13, -38, and -77. *cre*-mediated deletion of the selection cassette was verified for *csld2/6*KO-9 and 16 by amplification across the deletion site with primers D2KOFlankF/D2KOFlankR (2,724 bp). **(B)** Tube structures on *csld2/6*KO phyllids develop through altered cell expansion. Cells surrounding a cell separation (*) elongate radially forming an abaxial bulge with separation at the apex. Cell division and expansion enlarges the bulge forming a tube that protrudes from the abaxial surface. Scale bars = 50 µm. **(C)** CSLD2 or CSLD6 rescues phyllid development defects. Wild-type leaf morphology was restored when *csld2/6*KO plants were transformed with either a *CSLD2* or *CSLD6* expression vector, but not an empty control vector (EV). Ratios indicate the number of transformed lines with normal gametophores over the total number of transformed lines with gametophores. *csld2/6*KO image is a partial duplication of Fig. 2 G. **(D)** *CSLD2* and *CSLD6* are not required for protonemal development. Quantification of chlorophyll autofluorescence images of 7-d old wild type and *csld2/6*KO plants regenerated from protoplasts as a proxy for total plant area. A binary image of the median plant from each line is shown above (scale bar = 250 µm). For each of two experiments, 25 plants were measured from each of six replicate plates for each genetic line. Area was normalized to the wild-type parent line. Significant differences determined by a one-way ANOVA analysis with a Tukey post hoc test (alpha = 0.05) are indicated by different letters. Source data are available for this figure: SourceData FS2.

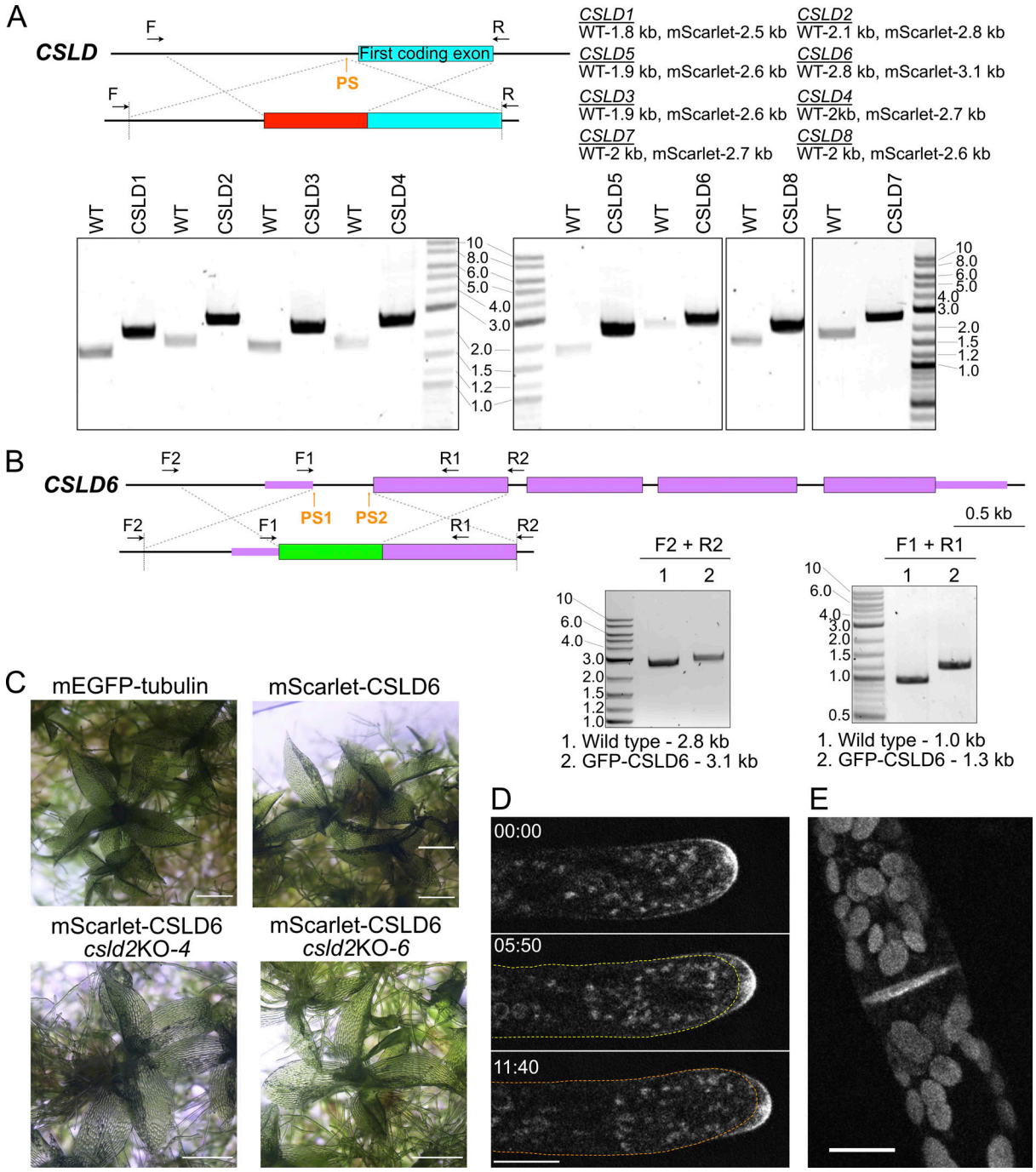

Figure S3. **Molecular characterization of the tagged *CSLD* loci. (A)** Diagram illustrates the result of HDR mediated insertion of mScarlet-i (red) sequence in a generic *CSLD* genomic locus. The position of the protospacer (PS) sequences is indicated with an orange arrow. The dashed vertical lines indicate the junction between the knock-in construct and upstream and downstream genomic sequences. Small arrows above the diagrams represent primers used for genotyping. PCR products obtained with the indicated primer pairs are shown below the diagram. Expected sizes for wild type (WT) and edited loci are shown for each *CSLD* locus. Molecular weight is indicated in kb. **(B)** Diagram illustrates the result of HDR mediated insertion of mEGFP (green) sequences in the *CSLD6* genomic locus. Coding exons are indicated by thick boxes and untranslated exons are indicated by thin boxes. Thin lines indicate intronic regions. The dashed vertical lines indicate the junction between the knock-in construct and upstream and downstream genomic sequences. Small arrows above the diagrams represent primers used for genotyping. Scale bar is 0.5 kb. PCR products obtained with the indicated primer pairs are shown below the diagram. Predicted sizes for correct products are indicated below each gel. Molecular weight is indicated in kb. **(C)** Gametophore phyllids form normally in 3–4-wk-old plants regenerated from ground tissue, with no phyllid patterning defects visible as seen in *csld2/6*KO plants (see Fig. 2, G and H), demonstrating that the tagged CSLD6 is functional. Scale bar, 500 µm. **(D)** Similar to mScarlet-CSLD6, mEGFP-CSLD6 is enriched in cytosolic punctae and at the apical plasma membrane of tip growing cells. Images are from a time lapse acquisition of confocal images of the medial plane of a growing protonemal cell. Time is indicated by min:sec. Yellow and orange dotted lines indicate the shape of the cell at 00:00, and 05:50 times, respectively. Scale bar, 10 µm. **(E)** Maximum projection of a confocal Z-stack of a dividing protonemal cell shows that mEGFP-CSLD6 accumulates at the cell division plane. Large globular structures are chloroplasts which are more concentrated near the division plane and auto-fluoresce in the GFP channel. Source data are available for this figure: SourceData FS3.

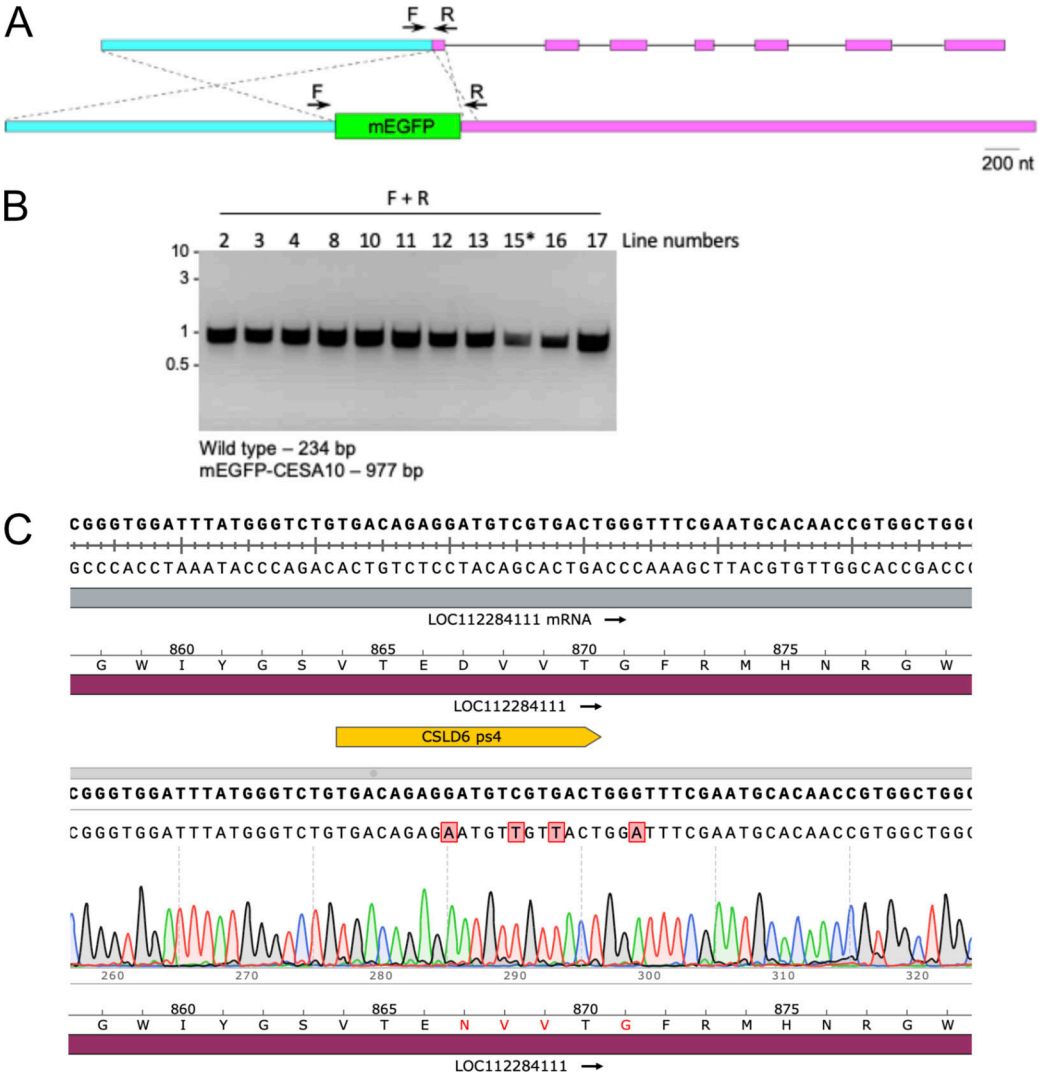

Figure S4. **Molecular characterization of the tagged *CESA10* locus and the mEGFP-CSLD6-TEN locus. (A)** Diagram illustrates the result of HDR mediated insertion of mEGFP sequences from the homology repair plasmid (bottom) into the *CESA10* genomic locus (top). Exons (first 7 shown) are indicated by pink boxes and the cloned promoter is indicated by cyan boxes. Thin lines indicate intronic regions. The inserted mEGFP sequence is denoted by a thick green box. Small arrows above the diagrams represent primers used for genotyping. **(B)** PCR products obtained with primer pairs using template DNA isolated from the indicated moss lines were separated on an agarose gel and stained with ethidium bromide. The asterisk indicates the line chosen for imaging after sequencing the PCR product. Molecular weight is indicated in kb. Predicted sizes for correct products are indicated below the gel. **(C)** Sequencing of a PCR product (Table S2) amplified from a plant transformed with PS4 (yellow bar) cloned into pMH-Cas9 together with double stranded TEN-oligo (Table S2) reveals CRISPR-Cas9 mediated editing resulting in the three designed silent mutations and the G2599A mutation resulting in D867N. Source data are available for this figure: SourceData FS4.

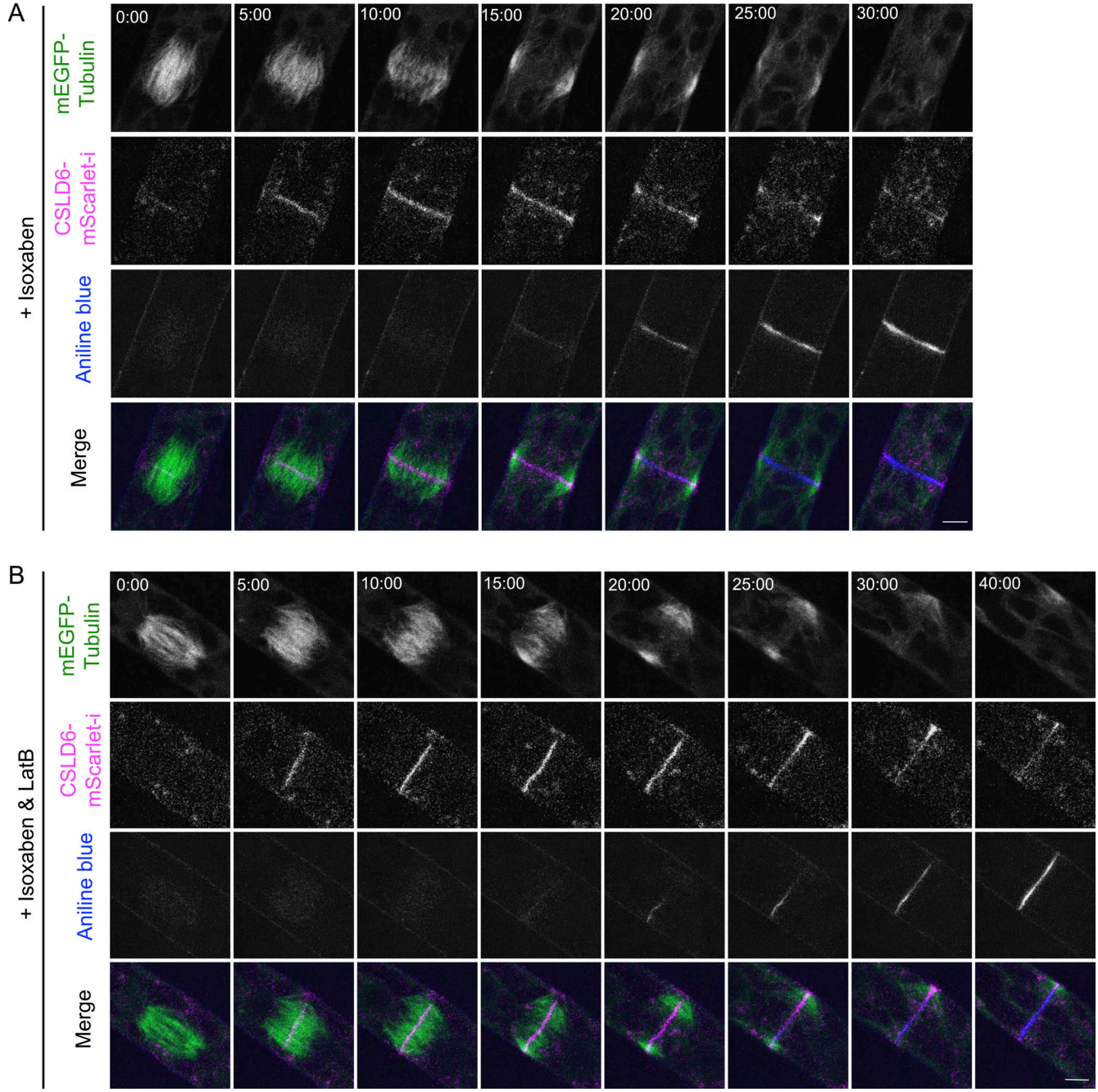

Figure S5. **Isoxaben does not affect cell plate formation.** Cell division in moss protonemata expressing mScarlet-CSLD6 (magenta in merge) and mEGFP-tubulin (green in merge), stained with aniline blue for callose (blue in merge). **(A)** Cell treated with 20 µM isoxaben. **(B)** Cell treated with 20 µM Isoxaben and 25 µM LatB. Images are single focal plane confocal images from a time-lapse acquisition. Scale bar, 5 µm. Time stamp, min:sec.

Video 1. **Wild-type gametophore expressing mScarlet-CLSD6.** Images are maximum projections of z-stacks acquired every 5 min on a laser scanning confocal microscope. Scale bar, 20 µm. Movie is playing at 8 fps. Also see Fig. 4 A.

Video 2. **Wild-type protonemata expressing Lifeact-mEGFP (green) and mScarlet-CLSD6 (magenta).** Images are maximum projections of z-stacks acquired every 5 min on a laser scanning confocal microscope. Scale bar, 20 µm. Movie is playing at 8 fps. Also see Fig. 4 B.

Video 3. **Wild-type protonemata expressing Lifeact-mEGFP (green) and mScarlet-CLSD6 (magenta).** Images are maximum projections of z-stacks acquired every 5 min on a laser scanning confocal microscope. Scale bar, 20 µm. Movie is playing at 8 fps. Also see Fig. 4 D.

Video 4. **Wild-type protonemata expressing Lifeact-mEGFP (green) and mScarlet-CLSD6 (magenta).** Images are single focal plane images acquired every 10 s on a laser scanning confocal microscope. Scale bar, 5 µm. Movie is playing at 8 fps. Also see Fig. 4 F.

Video 5. **Left, wild-type protonemata expressing GFP-CesA10, mEGFP-CLSD6, and mEGFP-CSLD6-TEN. Right, wild-type protonemata expressing mEGFP-CSLD treated with 20 µM isoxaben or 10 µM DCB.** Images are time-lapse VAEM acquired every 2 s. Scale bar, 2 µm. Movie is playing at 15 fps. Also see Fig. 5 A.

Video 6. **Wild-type protonemata expressing mScarlet-CLSD6 treated with no drug, 10 µM DCB, or 20 µM isoxaben.** The tip cell ruptured with DCB treatment. Images are single focal plane images acquired every 20 s on a laser scanning confocal microscope. Scale bar, 5 µm. Movie is playing at 8 fps. Also see Fig. 5, G and H.

Video 7. **Wild-type protonemata expressing GFP-tubulin (green) and mScarlet-CLSD6 (magenta).** Images are VAEM time-lapse acquired every 2 s. Scale bar, 2 µm. Movie is playing at 15 fps. Also see Fig. 6 A.

Video 8. **Cell division in tip cell with or without DCB treatment.** Wild-type protonemata expressing mEGFP-tubulin (green) and mScarlet-CLSD6 (magenta) were stained with aniline blue (blue). Images are single focal plane images acquired every minute on a laser scanning confocal microscope. Scale bar, 5 µm. Movie is playing at 8 fps. Also see Fig. 7, A and B.

Video 9. **Wild-type cell treated with 25 µM LatB undergoing cell division.** Wild-type protonemata expressing mEGFP-tubulin (green) and mScarlet-CLSD6 (magenta) were stained with aniline blue (blue). Images are single focal plane images acquired every minute on a laser scanning confocal microscope. Scale bar, 5 µm. Movie is playing at 8 fps. Also see Fig. 7 C.

Video 10. **Wild-type cell treated with 25 µM LatB and 10 µM DCB undergoing cell division.** Wild-type protonemata expressing mEGFP-tubulin (green) and mScarlet-CLSD6 (magenta) were stained with aniline blue (blue). Images are single focal plan images acquired every minute on a laser scanning confocal microscope. Scale bar, 5 µm. Movie is playing at 8 fps. Also see Fig. 7 D.

Provided online are Table S1, Table S2, and Table S3. Table S1 shows lines used in this study. Table S2 shows primers used for vector construction and genotype analysis. Table S3 shows *Physcomitrium patens* CSLD names and accession numbers.